Monthly Notices
of the
ROYAL ASTRONOMICAL SOCIETY

Mon. Not. R. Astron. Soc. **402,** 87–104 (2010) doi:10.1111/j.1365-2966.2009.15899.x

Kinematics of the parsec-scale radio jet in 3C 48

T. An,[1⋆] X. Y. Hong,[1] M. J. Hardcastle,[2,3] D. M. Worrall,[3] T. Venturi,[4] T. J. Pearson,[5] Z.-Q. Shen,[1] W. Zhao[1] and W. X. Feng[6]

[1] *Shanghai Astronomical Observatory, Chinese Academy of Sciences, 200030 Shanghai, China*
[2] *School of Physics, Astronomy and Mathematics, University of Hertfordshire, College Lane, Hatfield AL10 9AB*
[3] *Department of Physics, University of Bristol, Tyndall Avenue, Bristol BS8 1TL*
[4] *INAF – Istituto di Radioastronomia, I-40129, Bologna, Italy*
[5] *California Institute of Technology, Mail Stop 105-24, Pasadena, CA 91125, USA*
[6] *Liaocheng University, 252059 Liaocheng, China*

Accepted 2009 October 18. Received 2009 October 18; in original form 2009 September 10

ABSTRACT

We present results on the compact steep-spectrum quasar 3C 48 from observations with the Very Long Baseline Array (VLBA), the Multi-Element Radio Linked Interferometer Network (MERLIN) and the European Very long baseline interferometry (VLBI) Network (EVN) at multiple radio frequencies. In the 1.5-GHz VLBI images, the radio jet is characterized by a series of bright knots. The active nucleus is embedded in the southernmost VLBI component A, which is further resolved into two sub-components A1 and A2 at 4.8 and 8.3 GHz, respectively. A1 shows a flat spectrum and A2 shows a steep spectrum. The most strongly polarized VLBI components are located at component C ~ 0.25 arcsec north of the core, where the jet starts to bend to the north-east. The polarization angles at C show gradual changes across the jet width at all observed frequencies, indicative of a gradient in the emission-weighted intrinsic polarization angle across the jet and possibly a systematic gradient in the rotation measure; moreover, the percentage of polarization increases near the curvature at C, likely consistent with the presence of a local jet–interstellar-medium interaction and/or changing magnetic-field directions. The hot spot B shows a higher rotation measure, and has no detected proper motion. These facts provide some evidence for a stationary shock in the vicinity of B. Comparison of the present VLBI observations with those made 8.43 yr ago suggests a significant northward motion for A2 with an apparent transverse velocity $\beta_{\rm app} = 3.7 \pm 0.4c$. The apparent superluminal motion suggests that the relativistic jet plasma moves at a velocity of $\gtrsim 0.96c$ if the jet is viewed at an inclination angle less than 20°. A simple precessing jet model and a hydrodynamical isothermal jet model with helical-mode Kelvin–Helmholtz instabilities are used to fit the oscillatory jet trajectory of 3C 48 defined by the bright knots.

Key words: galaxies: active – galaxies: jets – galaxies: kinematics and dynamics – quasars: individual: 3C 48.

1 INTRODUCTION

Compact steep-spectrum (CSS) sources are a population of powerful radio sources with projected linear size less than 20 kpc and steep high radio frequency spectrum $\alpha < -0.5$[1] (Peacock & Wall 1982; Fanti et al. 1990, and review by O'Dea 1998; Fanti 2009). Kinematical studies of the hot spots and analysis of the high-frequency turnover in the radio spectrum due to radiative cooling imply ages for CSS sources in the range of 10^2–10^5 yr (e.g. Owsianik, Conway & Polatidis 1998; Murgia et al. 1999). The sub-galactic size of CSS sources has been used to argue that CSS sources are probably young radio sources (the 'youth' model; Fanti et al. 1995; Readhead et al. 1996). However, another interpretation attributes the apparent compactness of the CSS sources to being strongly confined by the dense interstellar medium (ISM) in the host galaxy (the 'frustration' model; van Breugel, Miley & Heckman 1984). Spectroscopic observations of CSS sources provide evidence for abundant gas reservoirs in the host galaxies and strong interaction between the radio sources and the emission-line clouds (O'Dea et al. 2002). Some CSS sources have been observed to have high-velocity

⋆E-mail: antao@shao.ac.cn
[1] In this paper, the spectral index is defined as $S_\nu \propto \nu^\alpha$.

clouds (as high as $\sim$500 km s^{-1}) in the narrow-line region (NLR), presumably driven by radio jets or outflows; an example is 3C 48 (Chatzichristou, Vanderriest & Jaffe 1999; Stockton et al. 2007). In addition, many CSS sources show distorted radio structures, suggestive of violent interaction between the jet and the ambient ISM (Wilkinson et al. 1984; Fanti et al. 1985; Akujor et al. 1991; Nan et al. 1991; Spencer et al. 1991; Nan et al. 1992). The ample supply of cold gas in their host galaxies and their strong radio activity, which results in a detection rate as high as $\sim$30 per cent in flux-density-limited radio source surveys (Peacock & Wall 1982; Fanti et al. 1990), make CSS sources good laboratories for the study of active galactic nuclei (AGN) triggering and feedback.

3C 48 ($z = 0.367$) is associated with the first quasar to be discovered (Matthews et al. 1961; Greenstein 1963) in the optical band. Its host galaxy is brighter than that of most other low redshift quasars. The radio source 3C 48 is classified as a CSS source due to its small size and steep radio spectrum (Peacock & Wall 1982). Optical and near-infrared (NIR) spectroscopic observations suggest that the active nucleus is located in a gas-rich environment and that the line-emitting gas clouds are interacting with the jet material (Canalizo & Stockton 1990; Stockton & Ridgway 1991; Chatzichristou et al. 1999; Zuther et al. 2004; Krips et al. 2005; Stockton et al. 2007). Very long baseline interferometry (VLBI) images (Wilkinson et al. 1990, 1991; Nan et al. 1991; Worrall et al. 2004) have revealed a disrupted jet in 3C 48, indicative of strong interactions between the jet flow and the dense clouds in the host galaxy. Although some authors (Wilkinson et al. 1991; Gupta, Srianand & Saikia 2005; Stockton et al. 2007) have suggested that the vigorous radio jet is powerful enough to drive massive clouds in the NLR at speeds up to 1000 km s^{-1}, the dynamics of the 3C 48 radio jet have yet to be well constrained. Due to the complex structure of the source, kinematical analysis of 3C 48 through tracing proper motions of compact jet components can only be done with VLBI observations at 4.8 GHz and higher frequencies, but until now the required multi-epoch high-frequency VLBI observations had not been carried out.

In order to study the kinematics of the radio jet for comparison with the physical properties of the host galaxy, we observed 3C 48 in a full polarization mode with the Very Long Baseline Array (VLBA) at 1.5, 4.8 and 8.3 GHz in 2004 and with the European VLBI Network (EVN) and Multi-Element Radio Linked Interferometer Network (MERLIN) at 1.65 GHz in 2005. Combined with earlier VLBA and EVN observations, these data allow us to constrain the dynamics of the jet on various scales. Our new observations and our interpretation of the data are presented in this paper. The remainder of the paper is laid out as follows. Section 2 describes the observations and data reduction, Section 3 presents the total intensity images of 3C 48 and Section 4 discusses the spectral properties and the linear polarization of the components of the radio jet. In Section 5, we discuss the implications of our observations for the kinematics and dynamics of the radio jet. Section 6 summarizes our results. Throughout this paper, we adopt a cosmological model with Hubble constant $H_0 = 70$ km s^{-1} Mpc^{-1}, $\Omega_{\rm m} = 0.3$ and $\Omega_\Lambda = 0.7$. Under this cosmological model, a 1-arcsec angular separation corresponds to a projected linear size of 5.1 kpc in the source frame at the distance of 3C 48 ($z = 0.367$).

2 OBSERVATIONS AND DATA REDUCTION

The VLBA observations [which included a single Very large Array (VLA) antenna] of 3C 48 were carried out at 1.5, 4.8 and 8.3 GHz on 2004 June 25. The EVN and MERLIN observations at 1.65 GHz were simultaneously made on 2005 June 7. Table 1 lists the parameters of the VLBA, EVN and MERLIN observations. In addition to our new observations, we made use of the VLBA observations described by Worrall et al. (2004) taken in 1996 at 1.5, 5.0, 8.4 and 15.4 GHz.

2.1 VLBA observations and data reduction

The total 12 h of VLBA observing time were evenly allocated among the three frequencies. At each frequency, the effective observing time on 3C 48 is about 2.6 h. The data were recorded at four observing frequencies (IFs) at 1.5 GHz and at two frequencies at the other two bands, initially split into 16 channels each, in a full polarization mode. The total bandwidth in each case was 32 MHz. The detailed data reduction procedure was as described by Worrall et al. (2004)

Table 1. Observational parameters of 3C 48.

Array[a]	VLBA	EVN	MERLIN
RA[b]	01 37 41.29943	01 37 41.29949	01 37 41.29675
Dec.[b]	33 09 35.1330	33 09 35.1338	33 09 35.5117
Date	2004 June 25	2005 June 7	2005 June 7
Time (UT)	08:00–20:00	02:00–14:00	02:00–14:00
τ (h)[c]	2.6/2.6/2.6	8.0	8.0
Freq. (GHz)[d]	1.5/4.8/8.3	1.65	1.65
BL (km)[e]	20–8600	130–8800	0.3–220
Calibrators	DA193, 3C138, 3C345	DA193, 3C138, 3C286	DA193, 3C138, 3C286, OQ208
BW (MHz)	32	32	15
Correlator	Socorro (VLBA)	JIVE (MK IV)	Jodrell Bank

[a]Participating EVN telescopes were Jodrell Bank (Lovell 76-m), Westerbork (phased array), Effelsberg, Onsala (25-m), Medicina, Noto, Torun, Shanghai, Urumqi, Hartebeesthoek and Cambridge; the MERLIN array consisted of Defford, Cambridge, Knockin, Darnhall, MK2, Lovell and Tabley; all 10 telescopes of the VLBA and a single VLA telescope participated in the VLBA observations.
[b]Pointing centre of the observations.
[c]Total integrating time on 3C 48.
[d]The central frequency of the observing band. The VLBA observations were carried out at three frequency bands of 1.5, 5 and 8 GHz.
[e]The projected baseline range of the array in thousands of wavelengths.

and was carried out in AIPS. We used models derived from our 1996 observations to facilitate fringe fitting of the 3C 48 data. Because the source structure of 3C 48 is heavily resolved at 4.8 and 8.3 GHz, and missing short baselines adds noise to the image, the initial data were not perfectly calibrated. We carried out self-calibration to further correct the antenna-based phase and amplitude errors. This progress improves the dynamic range in the final images.

Polarization calibration was also carried out in the standard manner. Observations of our bandpass calibrator, 3C 345, were used to determine the phase and delay offsets between the right- and left-handed polarization systems. The bright calibrator source DA 193 was observed at a range of parallactic angles and we used a model image of this, made from the Stokes *I* data, to solve for instrumental polarization. Our observing run included a snapshot observation of the strongly polarized source 3C 138. Assuming that the polarization position angle [or the E-Vector position angle (EVPA) in polarization images] of 3C 138 on VLBI scales at 1.5 GHz is the same as the value measured by the VLA, we used the measured polarization position angle of this source to make a rotation of 94° of the position angles in our 3C 48 data. We will later show that the corrected EVPAs of 3C 48 at 1.5 GHz are well consistent with those derived from the 1.65-GHz EVN data that are calibrated independently. At 4.8 GHz, 3C 138 shows multiple polarized components; we estimated the polarization angle for the brightest polarized component in 3C 138 from fig. 1 in Cotton et al. 2003 and determined a correction of −55° for the 3C 48 data. After the rotation of the EVPAs, the polarized structures at 4.8 GHz are basically in agreement with those at 1.5 GHz. At 8.3 GHz, the polarized emission of 3C 138 is too weak to be used to correct the absolute EVPA; we therefore did not calibrate the absolute EVPAs at 8.3 GHz.

2.2 EVN observations and data reduction

The effective observing time on 3C 48 was about 8 h. Apart from occasional radio frequency interference (RFI), the whole observation ran successfully. The data were recorded in four IFs. Each IF was split into 16 channels, each of 0.5-MHz channel width. In addition to 3C 48, we observed the quasars DA 193 and 3C 138 for phase calibration. 3C 138 was used as a fringe finder due to its high flux density of ∼9 Jy at 1.65 GHz.

The amplitude of the visibility data was calibrated using the system temperatures, monitored during the observations, and gain curves of each antenna that were measured within 2 weeks of the observations. The parallactic angles were determined on each telescope and the data were corrected appropriately before phase and polarization calibration. We corrected the ionospheric Faraday rotation using archival ionospheric model data from NASA's Crustal Dynamics Data Interchange System (CDDIS). DA 193 and OQ 208 were used to calibrate the complex bandpass response of each antenna. We first ran fringe fitting on DA 193 over a 10-min time-span to align the multiband delays. Then a full fringe fitting using all calibrators over the whole observing time was carried out to solve for the residual delays and phase rates. The gain solutions derived were interpolated to calibrate the 3C 48 visibility data. The single-source data were split for hybrid imaging. We first ran phase-only self-calibration of the 3C 48 data to remove the antenna-based, residual phase errors. Next, we ran three iterations of both amplitude and phase self-calibration to improve the dynamic range of the image.

DA 193 is weakly polarized at centimetre wavelengths (its fractional polarization is no more than 1 per cent at 5 GHz; Xiang et al. 2006), and was observed over a wide range of parallactic angles to calibrate the feed response to polarized signals. The instrumental polarization parameters of the antenna feeds (the so-called D-terms) were calculated from the DA 193 data and then used to correct the phase of the 3C 48 data. The absolute EVPA was then calibrated from the observations of 3C 138 (Cotton et al. 1997b; Taylor & Myers 2000). A comparison between the apparent polarization angle of 3C 138 and the value from the VLA calibrator monitoring programme (i.e. −15° at 20-cm wavelength) leads to a differential angle of −22°, which was applied to correct the apparent orientation of the E-vector for the 3C 48 data. After correction of instrumental polarization and absolute polarization angle, the cross-correlated 3C 48 data were used to produce Stokes *Q* and *U* images, from which maps of linear polarization intensity and position angle were produced.

2.3 MERLIN observations and data reduction

The MERLIN observations of 3C 48 were performed in the fake-continuum mode: the total bandwidth of 15 MHz was split into 15 contiguous channels, 1 MHz for each channel. A number of strong, compact extragalactic sources were interspersed into the observations of 3C 48 to calibrate the complex antenna gains.

The MERLIN data were reduced in AIPS following the standard procedure described in the MERLIN cookbook. The flux-density scale was determined using 3C 286 which has a flux density of 13.7 Jy at 1.65 GHz. The phases of the data were corrected for the varying parallactic angles on each antenna. Magnetized plasma in the ionosphere results in an additional phase difference between the right- and left-handed signals, owing to Faraday rotation. This time-variable Faraday rotation tends to defocus the polarized image and to give rise to erroneous estimates of the instrumental polarization parameters. We estimated the ionospheric Faraday rotation on each antenna based on the model suggested in the AIPS cookbook and corrected the phases of the visibilities accordingly. DA 193, OQ 208, PKS 2134+004 and 3C 138 were used to calibrate the time- and elevation-dependent complex gains. These gain solutions from the calibrators were interpolated to the 3C 48 data. The calibrated data were averaged in 30-s bins for further imaging analysis. Self-calibration in both amplitude and phase was performed to remove residual errors.

The observations of OQ 208 were used to calculate the instrumental polarization parameters of each antenna assuming a point-source model. The derived parameters were then applied to the multisource data. We compared the right- and left-hand phase difference of the 3C 286 visibility data with the phase difference value derived from the VLA monitoring program (i.e. 66° at 20 cm; Cotton et al. 1997b; Taylor & Myers 2000) and obtained a differential angle of 141°. This angle was used to rotate the EVPA of the polarized data for 3C 48.

2.4 Combination of EVN and MERLIN data

After self-calibration, the EVN and MERLIN data of 3C 48 were combined to make an image with intermediate resolution and high sensitivity. The pointing centre of the MERLIN observation was offset by 0.034 arcsec to the west and 0.378 arcsec to the north with respect to the EVN pointing centre (Table 1). Before combination, we first shifted the pointing centre of the MERLIN data to align with that of the EVN data. The Lovell and Cambridge telescopes took part in both the EVN and MERLIN observations. We compared the amplitude of 3C 48 on the common Lovell–Cambridge baseline in the EVN and MERLIN data and rescaled the EVN visibilities by

multiplying them by a factor of 1.4 to match the MERLIN flux. After combination of EVN and MERLIN visibility data, we performed a few iterations of amplitude and phase self-calibration to eliminate the residual errors resulting from minor offsets in registering the two coordinate frames and flux scales.

3 RESULTS – TOTAL INTENSITY IMAGES

Figs 1 and 2 exhibit the total intensity images derived from the MERLIN, VLBA and EVN data. The final images were created using the AIPS and MIRIAD software packages as well as the MAPPLOT program in the Caltech VLBI software package.

3.1 MERLIN images

Fig. 1 shows the total intensity image of 3C 48 from the MERLIN observations. We used the multifrequency synthesis technique to minimize the effects of bandwidth smearing, and assumed an optically thin synchrotron spectral index ($\alpha = -0.7$) to scale the amplitude of the visibilities with respect to the central frequency when averaging the data across multiple channels. The final image was produced using a hybrid of the Clark (BGC CLEAN) and Steer (SDI CLEAN) deconvolution algorithms. The image shows that the source structure is characterized by two major features: a compact component contributing about half of the total flux density (hereafter, referred to as the 'compact jet') and an extended component surrounding the compact jet like a cocoon (hereafter, called the 'extended envelope'). The compact jet is elongated in roughly the north–south direction, in alignment with the VLBI jet. The galactic nucleus corresponding to the central engine of 3C 48 is associated with the VLBI component A (Simon et al. 1990; Wilkinson et al. 1991). It is embedded in the southern end of the compact jet. The emission peaks at a location close to the VLBI jet component D; the second brightest component in the compact jet is located in the vicinity of the VLBI jet component B2 (Fig. 2, see Section 3.2). The extended envelope extends out to ∼1 arcsec north from the nucleus. At ∼0.25 arcsec north of the nucleus, the extended component bends and diffuses towards the north-east. The absence of short baselines ($uv < 30$ kλ) results in some negative features (the so-called negative bowl in synthesis images) just outside the outer boundary of the envelope.

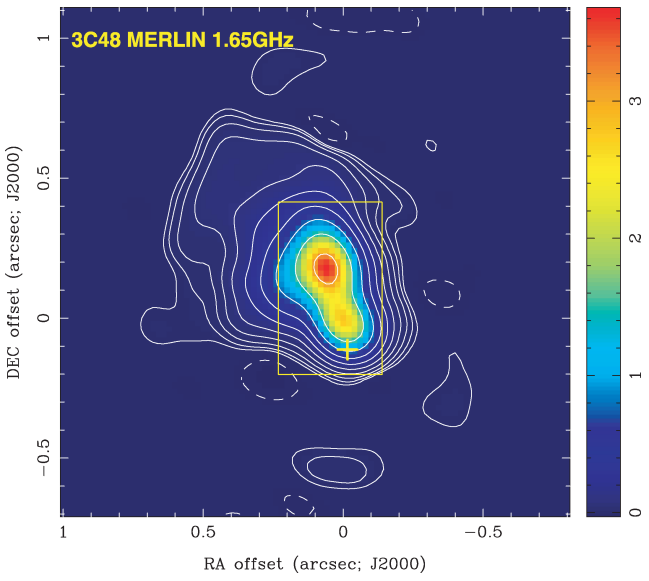

Figure 1. Total intensity (Stokes *I*) image of 3C 48 from the MERLIN observation at 1.65 GHz. The image was made with uniform weighting. The restoring beam is 138 × 115 (mas), PA = 65°.1. The phase centre is at RA = $01^{h}37^{d}41^{s}.29949$, dec. = +33°09′35″.1338. The rms noise in the image measured in an off-source region is ∼1.3 mJy beam^{-1}, corresponding to a dynamic range of ∼2800:1 in the image. The contours are 6 mJy b^{-1} × (−2, 1, 2, 4, . . . , 512). The cross denotes the location of the hidden AGN. The square marks the region in which the compact jet dominates the emission structure.

The integrated flux density over the whole source is 14.36 ± 1.02 Jy (very close to the single-dish measurement), suggesting that there is not much missing flux on short spacings. The uncertainty we assign includes both the systematic errors and the rms fluctuations in the image. Since the calibrator of the flux-density scale, 3C 286, is resolved on baselines longer than 600 kλ (Cotton et al. 1997a; An, Hong & Wang 2004), a model with a set of CLEAN components was used in flux-density calibration instead of a point-source model. We further compared the derived flux density of the phase calibrator DA 193 from our observations with published results (Condon et al. 1998; Stanghellini et al. 1998). The comparison suggests that the flux density of DA 193 from our MERLIN observation was consistent with that from the VLBI measurements to within 7 per cent. We note that this systematic error includes both the amplitude calibration error of 3C 286 and the error induced by the intrinsic long-term variability of DA 193; the latter is likely to be dominant.

The optical and NIR observations (Stockton & Ridgway 1991; Chatzichristou et al. 1999; Zuther et al. 2004) detect a secondary continuum peak, denoted 3C 48A, at ∼1 arcsec north-east of the optical peak of 3C 48. Although MERLIN would be sensitive to any compact structure with this offset from the pointing centre, we did not find any significant radio emission associated with 3C 48A. There is no strong feature at the position of 3C 48A even in high-dynamic-range VLA images (Briggs 1995; Feng et al. 2005). It is possibly due to the fact that the radio emission from 3C 48A is intrinsically weak if 3C 48A is a disrupted nucleus of the companion galaxy without an active AGN (Stockton & Ridgway 1991) or 3C 48A is an active star-forming region (Chatzichristou et al. 1999). In either case, the emission power of 3C 48A would be dominated by thermal sources and any radio radiation would be highly obscured by the surrounding ISM.

3.2 VLBA and EVN images

Fig. 2 shows the compact radio jet of 3C 48 on various scales derived from the VLBA and EVN observations. Table 2 gives the parameters of the images.

The VLBI data have been averaged on all frequency channels in individual IFs to export a single-channel data set. The visibility amplitudes on each IF have been corrected on the assumption of a spectral index of −0.7.

The total intensity images derived from the 1.5-GHz VLBA and 1.65-GHz EVN data are shown in Figs 2(a)–(c). The jet morphology we see is consistent with other published high-resolution images (Wilkinson et al. 1990, 1991; Nan et al. 1991; Worrall et al. 2004; Feng et al. 2005). The jet extends ∼0.5 arcsec in the north–south direction and consists of a diffuse plume in which a number of bright compact knots are embedded. We label these knots in the image using nomenclature consistent with the previous VLBI observations (Wilkinson et al. 1991; Worrall et al. 2004; we introduce the labels

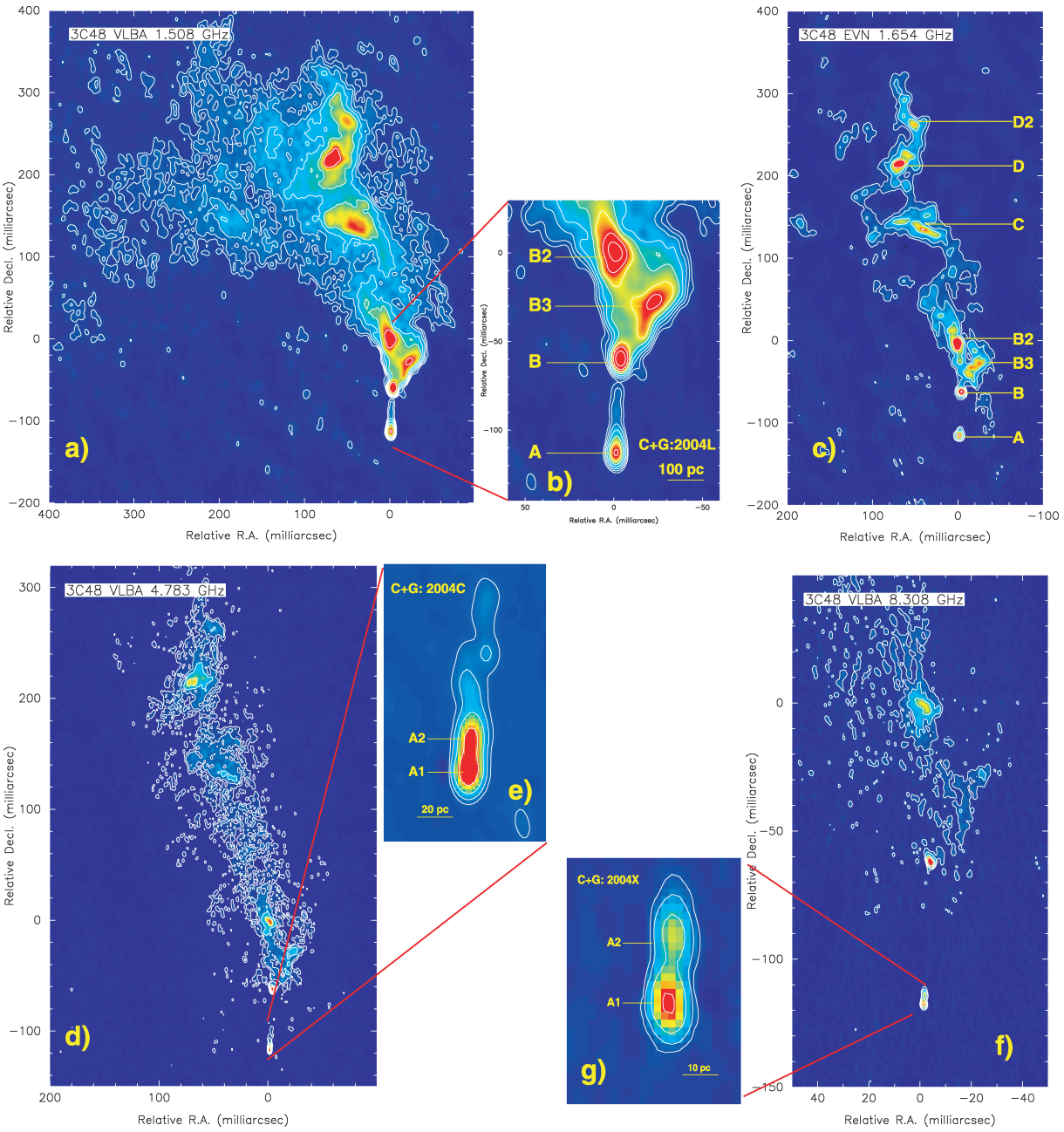

Figure 2. Total intensity (Stokes *I*) image of 3C 48 from VLBA and EVN observations. The phase centres of all images have been shifted to RA = $01^{\rm h}37^{\rm d}41\overset{\prime\prime}{.}29949$, dec. = $+33^{\circ}09'35\overset{\prime\prime}{.}1338$. Table 2 presents the image parameters. The horizon bars in the subpanels illuminates the length-scale in projection. A number of bright components are labelled in the images.

Table 2. Parameters of the total intensity maps of Fig. 2.

Label	Frequency (GHz)	Restoring beam Maj (mas)	Min (mas)	PA (°)	rms noise (mJy b^{-1})	Contours (mJy b^{-1})
Fig. 1	1.65	138	115	65.1	1.3	6.0 × (−2, 1, 2, 4, 8, . . ., 512)
Fig. 2(a)	1.51	8.3	5.3	1.0	0.25	1.0 × (1, 2, 4, 8, 16, 64, 256)
Fig. 2(b)	1.65	5.0	5.0	0.0	0.30	1.0 × (1, 4, 16, 64, 256)
Fig. 2(c)	4.78	2.7	1.7	0.0	0.040	0.16 × (1, 4, 16, 64, 256)
Fig. 2(d)	8.31	1.8	1.1	9.7	0.060	0.24 × (1, 4, 16, 64, 256)
Fig. 10[a]	1.65	16	10	−4.4	1.6	6.0 × (1, 4, 16, 32, 64, 128)

Note. All images are registered to the phase centre of the 2005 EVN image. [a]The parameters are for the 1.65-GHz EVN+MERLIN image in the right-hand panel.

B3 and D2 for faint features in the B and D regions, respectively, revealed by our new observations). The active nucleus is thought to be located at the southern end of the jet, i.e. close to the position of component A (Simon et al. 1990; Wilkinson et al. 1991). The bright knots, other than the nuclear component A, are thought to be associated with shocks that are created when the jet flow passes through the dense ISM in the host galaxy (Wilkinson et al. 1991; Worrall et al. 2004; Feng et al. 2005). Fig. 2(b) enlarges the inner jet region of C 48, showing the structure between A and B2. At $\sim$0.05 arcsec north away from the core A, the jet brightens at the hot spot B. B is in fact the brightest jet knot in the VLBI images. Earlier 1.5-GHz images (Fig. 1: Wilkinson et al. 1991; Fig. 5: Worrall et al. 2004) show only a weak flux ($\sim 4\sigma$) between A and B, but in our high-dynamic-range image in Fig. 2(b), a continuous jet is distinctly seen to connect A and B. From component B, the jet curves to the north-west. At $\sim$0.1 arcsec north of the nucleus, there is a bright component B2. After B2, the jet position angle seems to have a significant increase, and the jet bends into a second curve with a larger radius. At 0.25 arcsec north of the nucleus, the jet runs into a bright knot C which is elongated in the east–west direction. Here a plume of emission turns towards the north-east. The outer boundary of the plume feature is ill-defined in this image since its surface brightness is dependent on the rms noise in the image. The compact jet still keeps its northward motion from component C, but bends into an even larger curvature. Beyond component D2, the compact VLBI jet is too weak to be detected.

At 4.8 and 8.3 GHz, most of the extended emission is resolved out (Figs 2d–g) and only a few compact knots remain visible. Fig. 2(e) at 4.8 GHz highlights the core–jet structure within 150 pc ($\sim$30 mas); the ridge line appears to oscillate from side to side. At the resolution of this image the core A is resolved into two sub-components, which we denote A1 and A2. Fig. 2(g) at 8.3 GHz focuses on the nuclear region within 50 pc ($\sim$10 mas) and clearly shows two well-separated components. Beyond this distance, the brightness of the inner jet is below the detection threshold. This is consistent with what was seen in the 8.4- and 15.4-GHz images from the 1996 VLBA observations (Worrall et al. 2004).

Fig. 3 focuses on the core A and inner jet out to the hot spot B. Fig. 3(a) shows the 1.5-GHz image from 2004. Unlike the image already shown in Fig. 2(b), this image was produced with a super-uniform weighting of the uv plane (see the caption of Fig. 3 for details). The high-resolution 1.5-GHz image reveals a quasi-oscillatory jet extending to a distance of $\sim$40 mas ($\sim$200 pc) to the north of core A. Interestingly, Fig. 3(b) shows similar oscillatory jet structure at 4.8 GHz on both epoch 2004 (contours) and epoch 1996 (grey scale; Worrall et al. 2004). The consistency of the jet morphology seen in both 1.5- and 4.8-GHz images and in both epochs may suggest that the oscillatory pattern of the jet seen on kpc scales (Fig. 2) may be traced back to the innermost jet on parsec scales. Fig. 3(c) shows the 8.3-GHz images in 2004 (contours) and 1996 (grey scale; Worrall et al. 2004). In 1996 (the image denoted '1996X') the core is only slightly resolved into the two components A1 and A2, while these are well separated by 3.5 mas (two times the synthesized beam size) in the 2004 observations ('2004X'). Direct comparison of 1996X and 2004X images thus provides evidence for a northward position shift of A2 between 1996 and 2004. Fig. 3(d) overlays the 2004X contour map on the 1996U (15.4 GHz; Worrall et al. 2004) grey-scale map. Neglecting the minor positional offset of A1 between 1996U and 2004X, possibly due to opacity effects, this comparison of 1996U and 2004X maps is also consistent with the idea that A2 has moved north between 1996 and 2004. We will discuss the jet kinematics in detail in Section 4.5.

4 IMAGE ANALYSIS

4.1 Spectral index distribution along the radio jet

In order to measure the spectral properties of the 3C 48 jet, we remapped the 4.99-GHz MERLIN data acquired on 1992 June 15 (Feng et al. 2005) and compared it with the 1.65-GHz EVN+MERLIN data described in this paper. The individual data sets were first mapped with the same uv range and convolved with the same 40 × 40 (mas) restoring beam. Then we compared the intensities of the two images pixel by pixel to calculate the spectral index $\alpha_{1.65}^{4.99}$. The results are shown in Fig. 4. Component A shows a rather flat spectrum with a spectral index $\alpha_{1.65}^{4.99} = -0.24 \pm 0.09$. All other bright knots show steep spectral indices, ranging from -0.66 to -0.92. The extended envelope in general has an even steeper spectrum with $\alpha \lesssim -1.10$. Spectral steepening in radio sources is a signature of a less efficient acceleration mechanism and/or the depletion of high-energy electrons through synchrotron/Compton radiation losses and adiabatic losses as a result of the expansion of the plasma as it flows away from the active acceleration region. The different spectral index distribution seen in the compact jet and extended envelope may indicate that there are different electron populations in these two components, with the extended component arising from an aged electron population.

4.2 Linear polarization images

4.2.1 MERLIN images

Fig. 5 displays the polarization image made from the MERLIN data.

The majority of the polarized emission is detected in the inner region of the source, in alignment with the compact jet. The polarized intensity peaks in two locations. The brightest one is near the VLBI jet component C, with an integrated polarized intensity of 0.31 Jy and a mean percentage of polarization (defined as $\frac{\Sigma\sqrt{Q_i^2+U_i^2}}{\Sigma I_i}$, where i represents the ith polarized sub-components) of $m = 5.8$ per cent. The secondary one is located between VLBI jet components B and B2, with an integrated polarized intensity of 0.23 Jy and a mean degree of polarization $m = 9.5$ per cent. Both of the two peaks show clear deviations from the total intensity peaks in Fig. 1. These measurements of polarization structure and fractional polarization are in good agreement with those observed with the VLA at 2-cm wavelength with a similar angular resolution (van Breugel et al. 1984). The integrated polarized flux density in the whole source is 0.64 ± 0.05 Jy and the integrated fractional polarization is (4.9 ± 0.4) per cent. Since the integrated polarized intensity is in fact a vector sum of different polarized sub-components, the percentage polarization calculated in this way represents a lower limit. We can see from the image (Fig. 5) that the percentage of the polarization at individual pixels is higher than 5 per cent, and increases towards the south of the nucleus. A maximum value of $m \gtrsim 30$ per cent is detected at $\sim$0.045 arcsec south of the nucleus. The fractional polarization ($m > 4.9$ per cent) measured from our MERLIN observation at 18 cm is at least an order of magnitude higher than the VLA measurement at 20 cm, although it is consistent with the values measured by the VLA at 6 cm and shorter wavelengths. This difference in the fractional polarization at these very similar wavelengths is most likely to be an observational effect due to beam depolarization rather than being due to intrinsic variations in the Faraday depth (Perley, private communication).

The averaged polarization angle (or EVPA) is $-18^\circ \pm 5^\circ$ in the polarization structure. On the basis of the new measurements

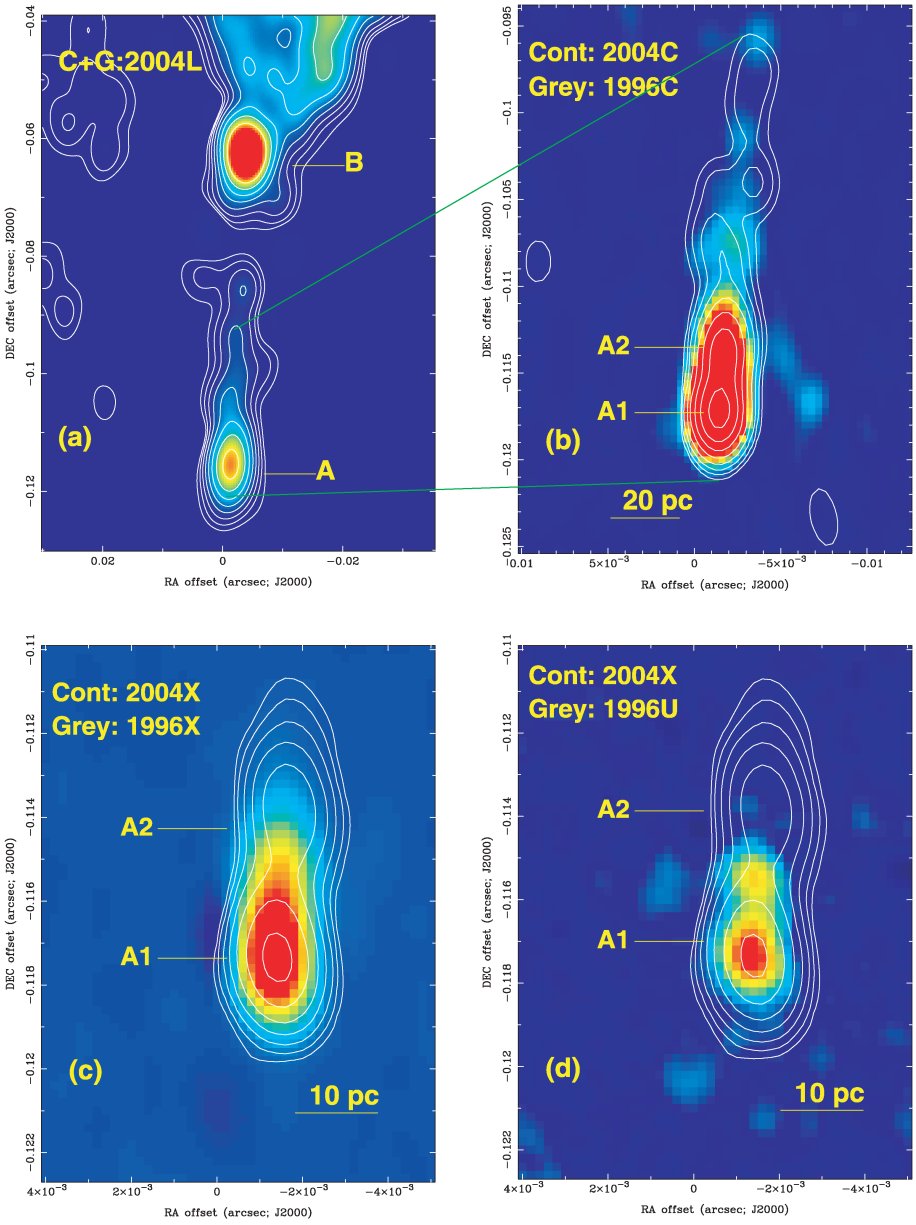

Figure 3. Total intensity (Stokes *I*) image of 3C 48 from VLBA observations in 2004 and 1996. Top left: 1.5-GHz image in epoch 2004. The image was made with a super-uniform weighting (ROBUST $= -4$ and UVBOX $= 3$ in AIPS task IMAGR) and restored with a beam of 6.2×3.9 (mas), PA $= -30^\circ$. Contours: 0.4 mJy b^{-1} $\times$ (1,2, ..., 128); top right: 4.8-GHz contours (epoch 1996) superposited on the grey-scale image (epoch 2004); bottom left: 8.3-GHz contours (epoch 2004) and grey scale (epoch 1996), bottom right: 8.3-GHz contours (epoch 2004) and 15.4-GHz grey scale (epoch 1996).

of the rotation measure (RM) towards 3C 48 by Mantovani et al. (2009), i.e. RM $= -64$ rad m^{-2} and intrinsic position angle $\phi_0 = 116^\circ$ (Simard-Normandin, Kronberg & Button 1981; Mantovani et al. 2009), we get a polarization angle of -4° at 1.65 GHz. This result suggests that the absolute EVPA calibration of 3C 48 agrees with the RM-corrected EVPA within 3σ. We show in Fig. 5 the RM-corrected EVPAs. The EVPAs are well aligned in the north–south direction, indicating an ordered magnetic field in the Faraday screen.

4.2.2 EVN and VLBA images

At the resolution of the EVN, most of the polarized emission from extended structures is resolved out. In order to map the polarized emission with modest sensitivity and resolution, we created Stokes *Q* and *U* maps using only the European baselines. Fig. 6(a) shows the linear polarization of 3C 48 from the 1.65-GHz EVN data. The polarized emission peaks at two components to the east (hereafter, 'C-East') and west (hereafter, 'C-West') of component C. The integrated polarized flux density is 24.8 mJy in 'C-West' and 22.9 mJy in 'C-East', and the mean percentage polarization in the two regions is 6.3 and 10.7 per cent, respectively. The real fractional polarization at individual pixels is much higher, for the reasons discussed in Section 4.2.1. There is clear evidence for the existence of sub-components in 'C-West' and 'C-East'; these polarized sub-components show a variety of EVPAs and have much higher fractional polarization than the 'mean' value. The polarization is as high as 40 per cent at the inner edge of knot C, which would

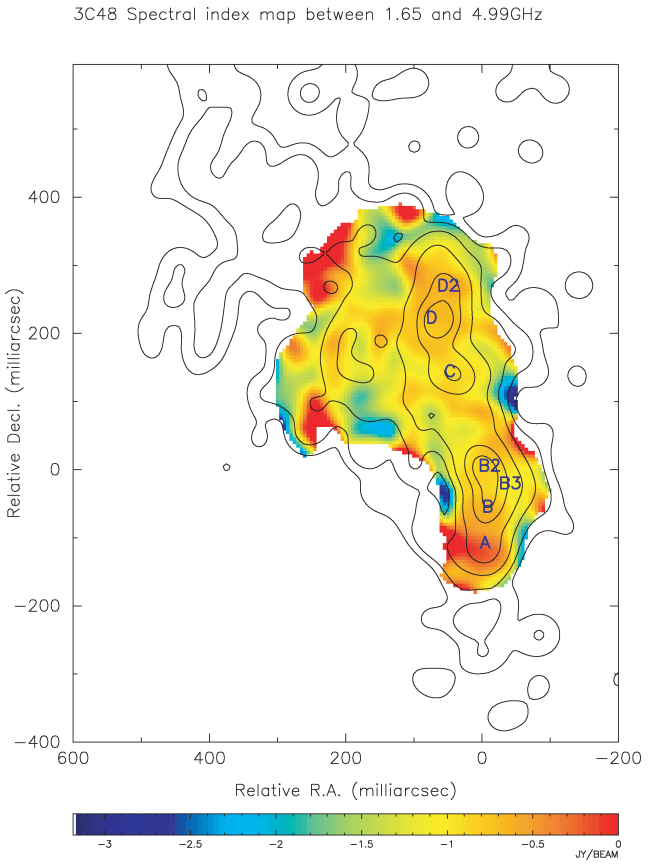

Figure 4. Spectral index map (grey scale) of 3C 48 between 1.65 and 4.99 GHz. The 4.99-GHz total intensity map (contours) is derived from the MERLIN observations on 1992 June 15 (Feng et al. 2005). The restoring beam of the 4.99-GHz image is 40 × 40 (mas). The lowest contour is 0.7 mJy b^{-1}, increasing in a step of 4. The 1.65-GHz data are obtained from the combined EVN and MERLIN data observed on 2005 June 7 (the present paper). The two images are re-produced using visibility data on the common uv range, and restored with the same 40 × 40 (mas) beam. Compact VLBI components are labelled in the image.

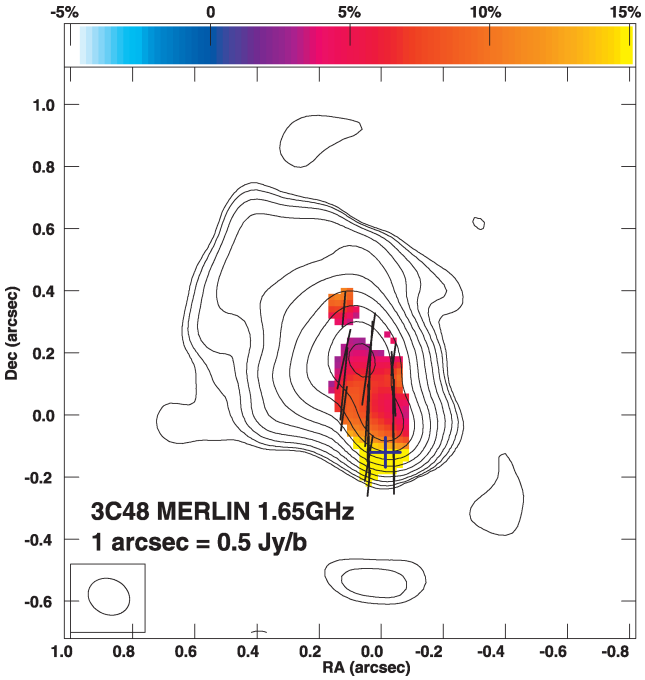

Figure 5. Polarization structure of 3C 48 from the MERLIN observations at 1.65 GHz. The contours map is Stokes I image (Fig. 1). The polarization image is derived from Stokes Q and U images above a 4σ cut-off (1σ = 6 mJy b^{-1}). The wedge at the top indicates the percentage of the polarization. The length of the bars represents the strength of polarized emission, 1 arcsec represents 0.5 Jy b^{-1}. The orientation of the bar indicates the RM-corrected EVPA.

be consistent with the existence of a shear layer produced by the jet–ISM interaction and/or a helical magnetic field (3C 43: Cotton et al. 2003; 3C 120: Gómez et al. 2008). Component B, the brightest VLBI component, however, is weakly polarized with an intensity of <4.0 mJy beam^{-1} (percentage polarization less than 1 per cent). The nucleus A shows no obvious polarization.

The 20-cm VLBA observations were carried out in four 8-MHz bands, centred at 1404.5, 1412.5, 1604.5 and 1612.5 MHz, respectively. In order to compare with the 1.65-GHz EVN polarization image, we made a VLBA polarization image (Fig. 6b) using data in the latter two bands. This image displays a polarization structure in excellent agreement with that detected at 1.65 GHz with the EVN, although the angular resolution is three times higher than the latter: the polarized emission mostly comes from the vicinity of component C and the fractional polarization increases where the jet bends; the hot spot B and the core A are weakly polarized or not detected in polarization. The 1.65- and 1.61-GHz images show detailed polarized structure in the component-C region on a spatial scale of tens of parsecs: the polarization angle (EVPA) shows a gradual increase across component C, with a total range of 160°, and the percentage of polarization gradually increases from 5 per cent to $\gtrsim$30 per cent from the western edge to the eastern edge at both 'C-West' and 'C-East'.

Figs 6(c) and (d) show the 4.8- and 8.3-GHz polarization images made with the VLBA data. Both images were made by tapering the visibility data using a Gaussian function in order to increase the signal-to-noise ratio of the low-surface brightness emission. Similar to what is seen in the 1.65- and 1.61-GHz images, component 'C-West' shows a polarization angle that increases by 80° across the component, but these images show the opposite sense of change of fractional polarization – fractional polarization decreases from 60 down to 20 per cent from the north-west to the south-east. Another distinct difference is that hot spot B shows increasing fractional polarization towards the higher frequencies, $m \sim 2.0$ per cent at 4.8 GHz and $m \sim 12$ per cent at 8.3 GHz in contrast with $m \lesssim 1$ per cent at 1.6 GHz. The difference in the fractional polarizations of B at 1.6/4.8 and 8.3 GHz imply that a component of the Faraday screen is unresolved at 1.6 and 4.8 GHz and/or that some internal depolarization is at work. The non-detection of polarization from the core A at all four frequencies may suggest a tangled magnetic field at the base of the jet.

4.3 EVPA gradient at component C and RM distribution

We found at all four frequencies that the polarization angles undergo a rotation by $\gtrsim$80° across the jet ridge line at both the 'C-East' and 'C-West' components. There are four possible factors that may affect the observed polarization angle: (1) the calibration of the absolute EVPAs, (2) Faraday rotation caused by Galactic ionized

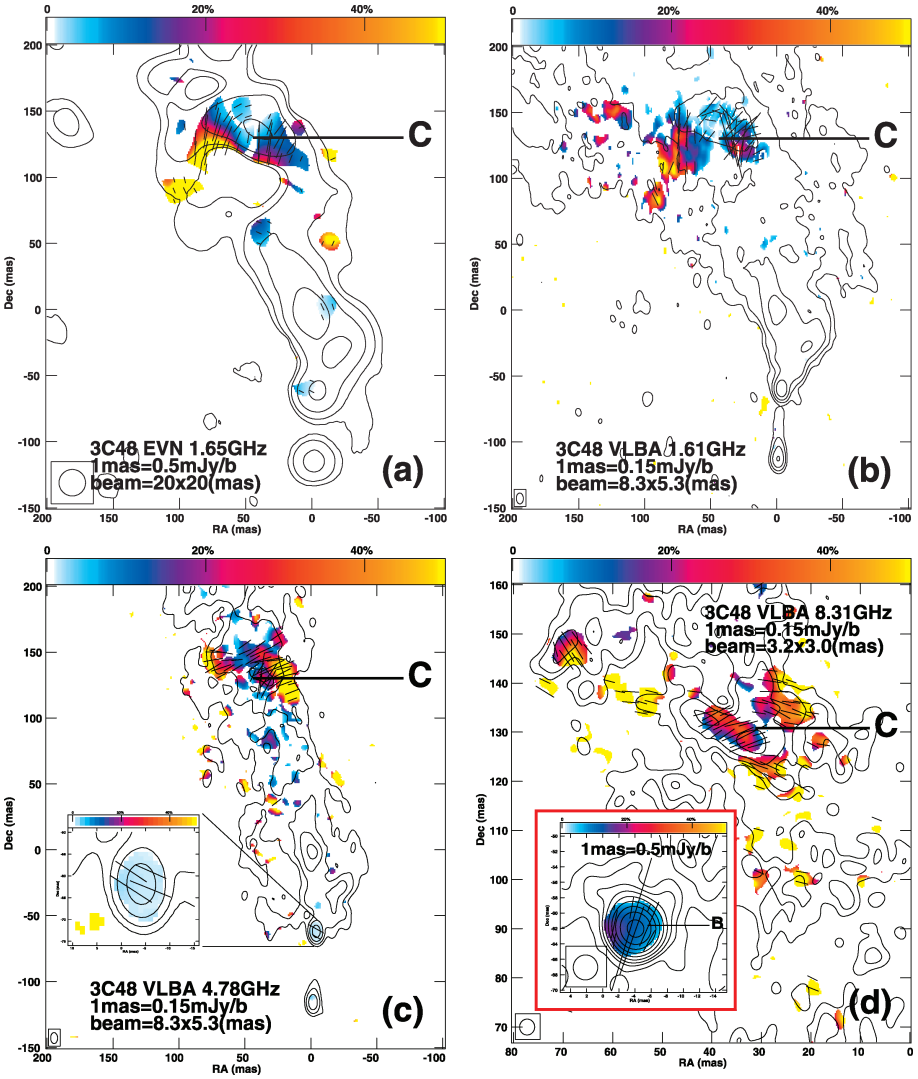

Figure 6. Polarization structure of 3C 48 derived from the EVN and VLBA data. The contours show the total intensity (Stoke I) emission and the grey scale indicates the fractional polarization. The length of the bars indicates the strength of the linear polarization intensity, and the orientation of the bars indicates the polarization angle, which has been corrected by the RM on the basis of the measurements by Mantovani et al. (2009). We should note that the VLBI images show more complex polarization structure than that shown in the MERLIN image (Fig. 5): quantitative calculations (Fig. 7) show that the RMs in the component-C region is about 1.4 times the value measured from the overall source; moreover, the intrinsic polarization angles rotate by $\sim$60° from the north-west edge of component C to the south-east edge. Therefore the correction based on the overall-source RM might not be sufficiently accurate to all sub-components, while this uncertainty tends to small towards the higher frequencies. (a) The EVN image at 1.65 GHz. Contours are 4 mJy b^{-1} × (1, 4, 16, 64, 256). The Stokes Q and U maps were convolved with a 20-mas circular beam, and we used intensities above 4σ to calculate the polarized intensity and polarization angle. (b) Contours: 1 mJy b^{-1} × (1, 4, 16, 64, 256). (c) Contours: 1 mJy b^{-1} × (1, 4, 16, 64, 256). (d) Contours: 1.2 mJy b^{-1} × (4, 16, 64, 256); the contours in the inset panel are 1.2 mJy b^{-1} × (1, 4, 8, 16, 32, 64, 128, 256, 512).

gas, (3) Faraday rotation due to gas within the 3C 48 system and (4) intrinsic polarization structure changes. The correction of absolute EVPAs applies to all polarization structure, so it cannot explain the position-dependent polarization angle changes at component C; in any case, the fact that we see similar patterns at four different frequencies, calibrated following independent procedures, rules out the possibility of calibration error. Galactic Faraday rotation is non-negligible (Section 4.2.1; -64 rad m^{-2} implies rotations from the true position angle of 168° at 1.4 GHz, 129° at 1.6 GHz, 14.°3 at 4.8 GHz and 4.°8 at 8.3 GHz) and means that we expect significant differences between the EVPA measured at our different frequencies; however, the Galactic Faraday screen should vary on much larger angular scales than what we observe. Only factors (3) and (4), which reflect the situation internal to the 3C 48 system itself, will give rise to a position-dependent rotation of the EVPAs. The EVPA gradient is related to the gradient of the RM and the intrinsic polarization angle by $\frac{\mathrm{d}\phi}{\mathrm{d}x} = \lambda^2 \frac{\mathrm{d(RM)}}{\mathrm{d}x} + \frac{\mathrm{d}\phi_0}{\mathrm{d}x}$, where the first term represents the RM gradient and the latter term represents the intrinsic polarization angle gradient. If the systematic gradient of EVPAs, $\frac{\mathrm{d}\phi}{\mathrm{d}x}$, were solely attributed to an RM gradient, then $\frac{\mathrm{d}\phi}{\mathrm{d}x}$ would show a strong frequency dependence; on the other hand, if $\frac{\mathrm{d}\phi}{\mathrm{d}x}$ is associated with the change of the intrinsic polarization angle, then there is no frequency dependence. We compared $\frac{\mathrm{d}\phi}{\mathrm{d}x}$ at 1.6 and 4.8 GHz and found a ratio $\frac{\mathrm{d}\phi/\mathrm{d}x(1.6\,\mathrm{GHz})}{\mathrm{d}\phi/\mathrm{d}x(4.8\,\mathrm{GHz})} = 1.8$. This number falls between 1.0 (the value expected if there were no RM gradient) and 8.8 (the ratio of λ^2), suggesting that a combination of RM and intrinsic polarization

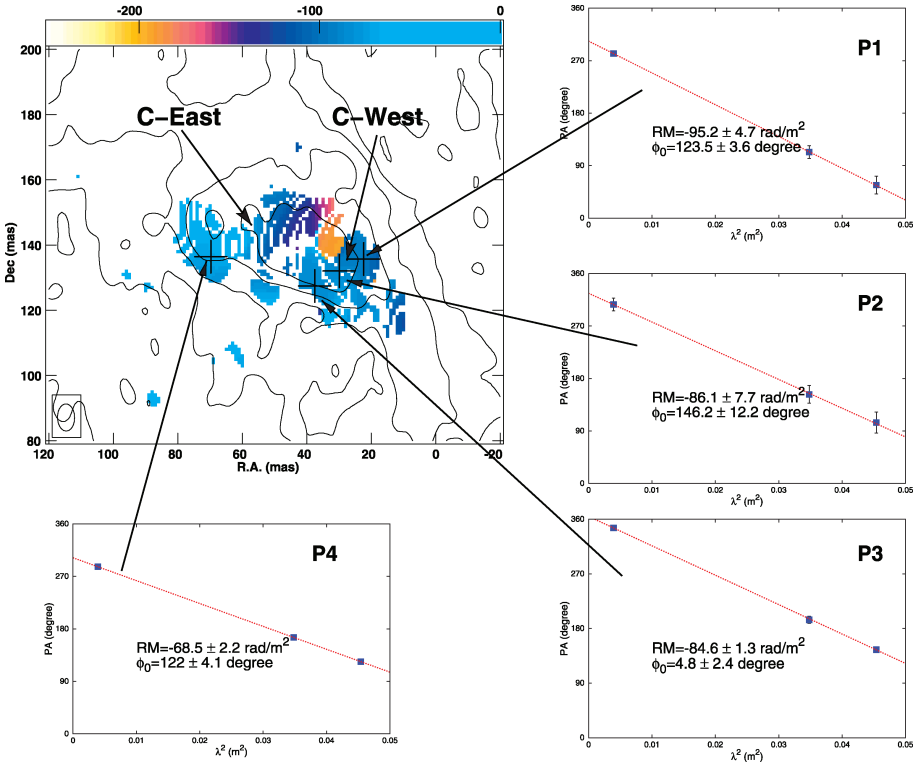

Figure 7. RM distribution in the component-C region. The patchy morphology is because at some pixels, polarization was not detected at all three frequencies simultaneously. The contours represent the total intensity: 1.0 mJy b^{-1} ×(1, 4, 8, 16). The wedge at the top indicates the RM in the observer's frame, in unit of rad m^{-2}. The insets show the measured values of the observed polarization angle for four selective locations as a function of λ^2 along with a linear fitting of RM.

angle gradients is responsible for the systematic gradient of EVPAs at C. Accordingly, it is worthwhile to attempt to measure the RM in the VLBI components of 3C 48.

The first two bands of the 20-cm VLBA data (centre frequency of 1.408 GHz) are separated from the last two bands (centre frequency of 1.608 GHz) by 200 MHz, indicating a differential polarization angle of ∼40° across the passband. The low integrated RM means that the effects of Faraday rotation are not significant (<10°) between 4.8 and 8.3 GHz, while the absolute EVPA calibration at 8.3 GHz is uncertain; moreover, the *uv* sampling at 8.3 GHz is too sparse to allow us to image identical source structure at 1.5 and 4.8 GHz. Therefore, we used the 1.408-, 1.608- and 4.78-GHz data to map the RM distribution in 3C 48.

We first re-imaged the Stokes Q and U data at the three frequencies with a common *uv* cut-off at >400 kλ and restored with the same convolving beam. We tapered the *uv* plane weights when imaging the 4.78-GHz data in order to achieve a similar intrinsic resolution to that of the images at the two lower frequencies. We then made polarization angle images from the Stokes Q and U maps. The three polarization angle images were assembled to calculate the RM (using AIPS task RM). The resulting RM image is shown in Fig. 7. The image shows a smooth distribution of RM in the component-C region except for a region north-east of 'C-West'. The superposed plots present the fits to the RM and intrinsic polarization angle (ϕ_0, the orientation of polarization extrapolated at $\lambda = 0$) at four selected locations. The polarization position angles at individual frequencies have multiples of π added or subtracted to remove the $n\pi$ ambiguity. The errors in the calculated RMs and ϕ_0 are derived from the linear fits. We note that the systematic error due to the absolute EVPA calibration feeds into the error on the observed polarization angle. All four fits show a good match with a λ^2 law. The fitted parameters at 'P4' in the 'C-East' region are consistent with those derived from the single-dish measurements for the overall source (Mantovani et al. 2009). The western component ('C-West') shows a gradient of RM from −95 rad m^{-2} at 'P1' to −85 rad m^{-2} at 'P3', and the intrinsic polarization angle varies from 123° (or −57°) at 'P1' through 146° (or −34°) at 'P2' to 5° at 'P3'. This result is in good agreement with the qualitative analysis of the EVPA gradients above. A straightforward interpretation of the gradients of the RMs and the intrinsic polarization angles is that the magnetic field orientation gradually varies across the jet ridge line; for example, a helical magnetic field surrounding the jet might have this effect. An alternative interpretation for the enhancement of the rotation measurement at the edge of the jet is that it is associated with thermal electrons in milliarcsec-scale Faraday screens surrounding or inside the jet due to jet–ISM interactions (Cotton et al. 2003; Gómez et al. 2008). More observations are needed to investigate the origins of the varying RM and ϕ_0.

The hot spot B shows a much larger difference of EVPAs between 4.8 and 8.3 GHz than is seen in component C. This might be a signature of different RMs at B and C. A rough calculation suggests an RM of -330 ± 60 rad m^{-2} at B. The high RM and high fractional polarization (Section 4.2) are indicative of a strong, ordered magnetic field in the vicinity of B. This might be expected in a region containing a shock in which the line-of-sight component of the magnetic field and/or the density of thermal electrons are enhanced; in fact, the proper motion of B (Section 4.5) does provide some evidence for a stationary shock in this region.

4.4 Physical properties of compact components in VLBI images

In order to make a quantitative study of the radiation properties of the compact VLBI components in 3C 48, we fitted the images of compact components in the VLBI images from our new observations and from the VLBA data taken in 1996 (Worrall et al. 2004) with Gaussian models. Measurements from the 1996 data used mapping parameters consistent with those for the 2004 images. Table 3 lists the fitted parameters of bright VLBI components in an ascending frequency order.

The discrete compact components in the 4.8- and 8.3-GHz VLBA images are well fitted with Gaussian models along with a zero-level base and slope accounting for the extended background structure. The fit to the extended emission structure is sensitive to the uv sampling and the sensitivity of the image. We have re-imaged the 1.5-GHz VLBA image using the same parameters as for the 1.65-GHz EVN image, i.e. the same uv range and restoring beam. At 1.5- and 1.65-GHz, Gaussian models are good approximations to the emission structure of compact sources with a high signal-to-noise ratio, such as components A and B. For extended sources (i.e. components B2 to D2) whose emission structures are either not well modelled by Gaussian distribution or blended with many sub-components, model fitting with a single Gaussian model gives a larger uncertainty for the fitted parameters. In particular, the determination of the integrated flux density is very sensitive to the apparent source size.

The uncertainties for the fitted parameters in Table 3 are derived from the output of the AIPS task JMFIT. These fitting errors are sensitive to the intensity fluctuations in the images and source shapes. In most cases, the fitting errors for the peak intensities of Gaussian components are roughly equal to the rms noise. We note that the uncertainty on the integrated flux density should also contain systematic calibration errors propagated from the amplitude calibration of the visibility data, in addition to the fitting errors. The calibration error normally dominates over the fitting error. The amplitude calibration for the VLBI antennas was made from the measurements of system temperature ($T_{\rm sys}$) at 2-min intervals during the observations combined with the antenna gain curves measured at each VLBI station. For the VLBA data, this calibration has an accuracy of $\lesssim$5 per cent of the amplitude scale.[2] Because of the diversity of the antenna performance of the EVN elements, we adopted an averaged amplitude calibration uncertainty of 5 per cent for the EVN data.

The positions of the VLBI core A1 at 4.8, 8.3 and 15.4 GHz show good alignment within 0.4 mas at different frequencies and epochs. The positions of the unresolved core A at 1.5 and 1.65 GHz show a systematic northward offset by 2–4 mas relative to the position of A1 at higher frequencies. Due to the low resolution and high opacity at 1.5 GHz, the position of A at this frequency reflects the centroid of the blended emission structure of the AGN and inner 40-pc jet. The parameters that we have derived for the compact components A, B and B2 in epoch 1996 are in good agreement with those determined by Worrall et al. (2004) at the same frequency band. The results for fitting to extended knots at 1.5 and 1.65 GHz are in less good agreement. This is probably because of the different uv sampling on short spacings, meaning that the VLBA and EVN data sample different extended structures in the emission.

[2] See the online VLBA status summary at http://www.vlba.nrao.edu/astro/obstatus/current/obssum.html.

The integrated flux densities of the VLBI components A1 and A2 in 1996X (8.3 GHz) are higher than those in 2004X (8.3 GHz) by $\sim$100 per cent (A1) and $\sim$60 per cent (A2), respectively. The large discrepancy in the flux densities of A1 and A2 between epochs 1996X and 2004X cannot easily be interpreted as an amplitude calibration error of larger than 60 per cent since we do not see a variation at a comparable level in the flux densities of components B, B2 and D. Although the *total* flux densities of CSS sources in general exhibit no violent variability at radio wavelengths, the possibility of small-amplitude ($\lesssim$100 per cent) variability in the VLBI core and inner jet components is not ruled out.

Component A1 has a flat spectrum with $\alpha_{4.8}^{8.3} = -0.34 \pm 0.04$ between 4.8 and 8.3 GHz in epoch 2004; component A2 has a rather steeper spectrum with $\alpha_{4.8}^{8.3} = -1.29 \pm 0.16$ (epoch 2004). The spectral properties of these two components support the idea that A1 is associated with the active nucleus and suffers from synchrotron self-absorption at centimetre radio wavelengths; in this picture, A2 is the innermost jet. The spectral indices of components B and B2 in epoch 2004 are $\alpha_{4.8}^{8.3} = -0.82 \pm 0.10$ (B) and $\alpha_{4.8}^{8.3} = -0.79 \pm 0.10$ (B2), respectively. This is consistent with the measurements from the 1.65- and 4.99-GHz images (Fig. 4). Component D shows a relatively flatter spectrum in epoch 2004 with $\alpha_{4.8}^{8.3} = -0.46 \pm 0.06$, in contrast to the other jet knots. While this spectral index is consistent with those of the shock-accelerated hot spots in radio galaxies, the flattening of the spectrum in D might also arise from a local compression of particles and magnetic field.

Table 4 lists the brightness temperatures ($T_{\rm b}$) of the compact VLBI components A1, A2 and B. All these VLBI components have a brightness temperature ($T_{\rm b}$) higher than 10^8 K, confirming their non-thermal origin. These brightness temperatures are well below the 10^{11-12} K upper limit constrained by the inverse Compton catastrophic (Kellermann & Pauliny-Toth 1969), suggesting that the relativistic jet plasma is only mildly beamed towards the line of sight. The $T_{\rm b}$ of A1 is about three times higher than that of A2 at 4.8 and 8.3 GHz and the $T_{\rm b}$ of A1 decreases towards higher frequencies. Together with the flat spectrum and variability of A1, the observed results are consistent with A1 being the self-absorbed core harbouring the AGN. $T_{\rm b}$ is much higher in 1996X than 2004X for both A1 and A2, a consequence of the measured flux-density variation between the two epochs.

4.5 Proper motions of VLBI components

The Gaussian fitting results presented in Table 3 may be used to calculate the proper motions of VLBI components. In order to search for proper motions in 3C 48, maps at different epochs should be aligned at a compact component such as the core (Worrall et al. 2004). However, thanks to our new VLBI observations we know that aligning the cores at 1.5 GHz is not likely to be practical, since the core structure appears to be changing on the relevant timescales. Even at 4.8 GHz, the core still blends with the inner jet A2 in epoch 1996C (Fig. 3). In contrast to these two lower frequencies, the 8.3-GHz images have higher resolution, better separation of A1 and A2, and less contamination from extended emission. These make 8.3-GHz images the best choice for the proper motion analysis. In the following discussion of proper motion measurements, we rely on the 8.3-GHz images.

We have already commented on the shift of the peak of A2 to the north from epochs 1996X to 2004X in Fig. 3. A quantitative calculation based on the model fitting results gives a positional variation of 1.38 mas to the north and 0.15 mas to the west during a time-span 8.43 yr, assuming that the core A1 is stationary. This corresponds to

Table 3. Properties of bright components in Fig. 2.

Freq. (GHz) (1)	Comp. (2)	RA(J2000)[a] (^{h}, ^{m}, ^{s}) (3)	Dec.(J2000)[a] ($^\circ$, $'$, $''$) (4)	S_p (mJy b^{-1}) (5)	S_i (mJy) (6)	θ_{maj} (mas) (7)	θ_{min} (mas) (8)	PA ($^\circ$) (9)
				1996 January 20 (1996L)				
1.53	A	01 37 41.2994260	33 09 35.021073	59.94 ± 0.84	93.29 ± 1.97	4.77 ± 0.14	2.58 ± 0.18	173.0 ± 2.7
	B	−2.69	53.61	153.56 ± 0.84	224.45 ± 1.89	4.02 ± 0.06	2.72 ± 0.07	157.2 ± 1.8
	B2	0.58	113.73	93.20 ± 0.78	529.51 ± 5.17	13.46 ± 0.13	8.53 ± 0.10	22.8 ± 0.8
	B3	−20.97	84.80	37.04 ± 0.78	309.78 ± 7.23	20.38 ± 0.45	8.62 ± 0.24	131.8 ± 1.0
	C	37.56	247.68	24.42 ± 0.62	385.70 ± 10.30	27.94 ± 0.73	12.98 ± 0.38	70.1 ± 1.3
	D	70.64	331.18	86.88 ± 0.78	518.96 ± 5.40	14.39 ± 0.15	8.43 ± 0.10	123.7 ± 0.8
	D2	50.59	378.93	21.07 ± 0.76	219.28 ± 8.62	19.56 ± 0.75	11.87 ± 0.51	31.4 ± 3.1
				2004 June 25 (2004L)				
1.51	A	01 37 41.2993864	33 09 35.018436	72.33 ± 0.71	99.91 ± 1.53	4.87 ± 0.14	0.00 ± 0.00	173.2 ± 1.1
	B	−2.57	52.94	264.06 ± 0.72	308.76 ± 1.38	2.56 ± 0.06	1.43 ± 0.05	0.7 ± 1.4
	B2	0.73	112.98	130.17 ± 0.66	657.32 ± 3.92	13.17 ± 0.13	7.43 ± 0.06	20.6 ± 0.4
	B3	−21.79	84.88	47.78 ± 0.65	371.90 ± 5.67	18.56 ± 0.45	8.80 ± 0.16	127.6 ± 0.8
	C	38.82	246.04	28.84 ± 0.57	376.94 ± 7.94	28.05 ± 0.73	10.31 ± 0.25	65.4 ± 0.8
	D	70.82	329.60	119.13 ± 0.66	616.05 ± 3.99	13.49 ± 0.15	7.46 ± 0.06	125.4 ± 0.5
	D2	50.52	377.20	26.99 ± 0.65	235.54 ± 6.27	18.01 ± 0.75	10.54 ± 0.31	62.5 ± 2.0
				2005 June 7 (2005L)				
1.65	A	01 37 41.2993690	33 09 35.018826	75.23 ± 0.29	108.27 ± 0.64	4.94 ± 0.04	1.09 ± 0.10	178.0 ± 0.5
	B	−2.56	52.92	279.84 ± 0.30	318.86 ± 0.56	2.40 ± 0.01	1.18 ± 0.02	23.7 ± 0.6
	B2	2.24	111.56	155.31 ± 0.27	771.75 ± 1.59	13.44 ± 0.03	7.08 ± 0.02	12.1 ± 0.1
	B3	−20.48	85.23	50.78 ± 0.27	297.29 ± 1.82	17.98 ± 0.10	6.04 ± 0.05	126.9 ± 0.2
	C	40.60	249.55	53.14 ± 0.27	388.12 ± 2.20	26.65 ± 0.14	4.51 ± 0.05	62.6 ± 0.1
	D	70.31	329.77	190.60 ± 0.28	597.33 ± 1.10	9.79 ± 0.02	5.08 ± 0.02	109.9 ± 0.1
	D2	53.48	377.67	46.10 ± 0.27	186.20 ± 1.34	11.92 ± 0.08	6.00 ± 0.06	40.6 ± 0.4
				1996 January 20 (1996C)				
4.99	A	01 37 41.2993853	33 09 35.016904	46.80 ± 0.04	60.77 ± 0.08	1.80 ± 0.01	0.43 ± 0.01	174.4 ± 0.1
	B	−2.71	54.85	88.73 ± 0.04	135.70 ± 0.08	2.11 ± 0.01	1.37 ± 0.01	36.3 ± 0.2
	B2	0.19	115.75	17.99 ± 0.03	162.30 ± 0.34	9.37 ± 0.02	4.99 ± 0.01	44.8 ± 0.1
	B3	−22.32	90.35	4.04 ± 0.03	46.77 ± 0.39	10.21 ± 0.08	6.21 ± 0.06	149.3 ± 0.7
	D	71.33	331.53	11.75 ± 0.02	300.35 ± 0.56	15.82 ± 0.03	9.28 ± 0.02	121.1 ± 0.1
				2004 June 25 (2004C)				
4.78	A1	01 37 41.2993814	33 09 35.016523	26.75 ± 0.05	28.80 ± 0.10	1.00 ± 0.02	0.56 ± 0.02	176.3 ± 2.2
	A2	−0.28	3.39	16.69 ± 0.05	22.86 ± 0.11	2.97 ± 0.02	0.57 ± 0.03	175.7 ± 0.3
	B	−2.63	55.19	105.06 ± 0.05	140.80 ± 0.11	2.00 ± 0.01	0.96 ± 0.01	39.8 ± 0.2
	B2	−0.02	116.06	23.11 ± 0.05	161.84 ± 0.37	9.12 ± 0.02	4.61 ± 0.02	42.9 ± 0.2
	B3	−22.39	90.01	4.07 ± 0.04	52.92 ± 0.57	12.42 ± 0.13	6.92 ± 0.09	112.9 ± 0.8
	D	71.39	331.59	14.88 ± 0.03	322.44 ± 0.72	16.36 ± 0.04	9.22 ± 0.03	121.1 ± 0.2
				1996 January 20 (1996X)				
8.41	A1	01 37 41.2993871	33 09 35.016521	30.55 ± 0.06	47.91 ± 0.15	1.39 ± 0.01	0.22 ± 0.01	176.0 ± 0.2
	A2	−0.14	2.03	11.30 ± 0.06	18.27 ± 0.15	1.39 ± 0.03	0.34 ± 0.02	174.0 ± 0.5
	B	−2.73	55.20	46.00 ± 0.06	89.00 ± 0.17	1.38 ± 0.01	0.71 ± 0.01	46.8 ± 0.3
	B2	−0.34	115.65	5.04 ± 0.05	96.36 ± 0.86	6.08 ± 0.06	3.54 ± 0.03	46.2 ± 0.5
	D	71.46	331.98	4.41 ± 0.02	271.57 ± 1.46	13.10 ± 0.07	8.09 ± 0.04	121.5 ± 0.4
				2004 June 25 (2004X)				
8.31	A1	01 37 41.2993822	33 09 35.016514	18.09 ± 0.06	23.85 ± 0.12	1.18 ± 0.01	0.38 ± 0.02	178.7 ± 0.6
	A2	−0.29	3.41	6.89 ± 0.05	11.19 ± 0.14	1.80 ± 0.03	0.41 ± 0.04	175.1 ± 0.8
	B	−2.63	55.24	55.84 ± 0.06	89.38 ± 0.14	1.34 ± 0.01	0.72 ± 0.01	37.8 ± 0.3
	B2	−0.12	116.13	6.61 ± 0.04	104.47 ± 0.74	7.14 ± 0.05	3.60 ± 0.03	43.4 ± 0.4
	D	70.99	331.82	4.16 ± 0.02	250.24 ± 1.39	13.11 ± 0.07	7.89 ± 0.04	120.8 ± 0.4
				1996 January 20 (1996U)				
15.36	A1	01 37 41.2993868	33 09 35.016511	9.22 ± 0.20	14.59 ± 0.48	1.05 ± 0.04	0.44 ± 0.06	11.3 ± 3.0
	A2	−0.10	1.76	5.48 ± 0.18	7.50 ± 0.44	0.93 ± 0.08	0.20 ± 0.04	19.4 ± 5.0
	B	−2.72	55.20	16.27 ± 0.17	27.83 ± 0.51	1.18 ± 0.03	0.47 ± 0.03	41.8 ± 1.6
	B2	−0.07	116.01	1.63 ± 0.14	29.50 ± 2.65	6.59 ± 0.57	2.52 ± 0.25	39.8 ± 3.3

[a]For individual data sets, the right ascension and declination positions of the nuclear component A (A1) in the J2000.0 coordinate frame are presented. The relative positions of jet components are given with respect to the nuclear component A (A1).

a proper motion of $\mu_\alpha = -0.018 \pm 0.007$ mas yr^{-1} ('minus' mean moving to the west) and $\mu_\delta = 0.164 \pm 0.015$ mas yr^{-1}, corresponding to an apparent transverse velocity of $v_\alpha = -0.40 \pm 0.16c$ and $v_\delta = 3.74 \pm 0.35c$. The error quoted here includes both the positional uncertainty derived from the Gaussian fitting and the relative offset of the reference point (i.e. A1). That means that we detect a significant ($>10\sigma$) proper motion for A2 moving to the north. The apparent transverse velocity for A2 is similar to velocities derived

Table 4. Brightness temperature (T_b) of compact VLBI components.

T_b	A1	A2	B
2004C	37.4	9.8	53.4
1996X	74.2	8.9	17.2
2004X	12.8	3.7	22.4
1996U	2.2	2.7	23.2

Note. T_b are given in units of 10^8 K.

from other CSS and gigahertz peaked-spectrum sources in which apparent superluminal motions in the pc-scale jet have been detected, e.g. 3.3–9.7c in 3C 138 (Cotton et al. 1997b; Shen et al. 2001).

We also searched for evidence for proper motions of the other jet knots. The proper motion measurement is limited by the accuracy of the reference point alignment, our ability to make a high-precision position determination at each epoch and the contamination from the extended structure. We found only a 3σ proper motion from B2, which shows a position change of $\Delta\alpha = 0.22 \pm 0.07$ mas and $\Delta\delta = 0.48 \pm 0.13$ mas in 8.43 yr, corresponding to an apparent velocity of $\beta_{\rm app} = 1.43 \pm 0.33c$ to the north-east. The measurements of the position variation of the hot spot B between 1996X and 2004X show no evidence for proper motion with $\mu_\alpha = 0.012 \pm 0.007$ mas yr^{-1} and $\mu_\delta = 0.005 \pm 0.015$ mas yr^{-1}. Worrall et al. (2004) earlier reported a 3σ proper motion for B by comparing the 1.5-GHz VLBA image taken in 1996 with Wilkinson et al's 1.6-GHz image taken 11.8 yr ago. However, as mentioned above, the 1.5-GHz measurements are subject to the problems of lower angular resolution, poor reference point alignment and contamination from structural variation. In particular, if we extrapolate the observed angular motion of A2 back, the creation of jet component A2 took place in 1984, therefore in 1996 A2 would still have been blended with A1 in the 1.5-GHz image within $\frac{1}{4}$ beam. The fitting of a Gaussian to the combination of A1 and A2 at 1.5 GHz on epoch 1996 would then have suffered from the effects of the structural changes in the core due to the expansion of A2. For these reasons, we conclude that the hot spot B is stationary to the limit of our ability to measure motions. For the other jet components, the complex source structure does not permit any determination of proper motions.

5 KINEMATICS OF THE RADIO JET

5.1 Geometry of the radio jet

Most CSS sources show double or triple structures on kpc scales, analogous to classical Fanaroff–Riley type I (FR I) or FR II galaxies. However, some CSS sources show strongly asymmetric structures. At small viewing angles, the advancing jet looks much brighter than the receding one, due to Doppler boosting. The sidedness of radio jets can be characterized by the jet-to-counterjet intensity ratio R. In VLA images (Briggs 1995; Feng et al. 2005), 3C 48 shows two-sided structure in the north–south direction. The southern (presumably receding) component is much weaker than the north (advancing) one. In VLBI images (Wilkinson et al. 1991; Worrall et al. 2004; this paper), 3C 48 shows a one-sided jet to the north of the nucleus. If the non-detection of the counterjet is solely attributed to Doppler deboosting, the sideness parameter R can be estimated from the intensity ratio of jet knots to the detection limit (derived from the 3σ off-source noise). Assuming the source is intrinsically symmetric out to a projected separation of 600 pc (the distance of B2 away from A1), the sideness parameter would be >200 for B2 and B in the 1.5-GHz image (Fig. 2a). In the highest sensitivity image on epoch 2004C (Fig. 2d), the off-source noise in the image is 40 μJy beam^{-1}, so that the derived R at component B could be as high as $\gtrsim$900.

For a smooth jet which consists of a number of unresolved components, the jet-to-counterjet brightness ratio R is related to the jet velocity (β) and viewing angle (Θ) by

$$R = \left(\frac{1+\beta\cos\Theta}{1-\beta\cos\Theta}\right)^{2-\alpha}.$$

Assuming an optically thin spectral index $\alpha = -1.0$ for the 3C 48 jet (Fig. 4), the sideness parameter $R \gtrsim 900$ estimated above gives a limit of $\beta\cos\Theta > 0.81c$ for the projected jet velocity in the line of sight. Using only the combination of parameters $\beta\cos\Theta$, it is not possible to determine the kinematics (jet speed β) and the geometry (viewing angle Θ) of the jet flow. Additional constraints may come from the apparent transverse velocity, which is related to the jet velocity by $\beta_{\rm app} = \frac{\beta\sin\Theta}{1-\beta\cos\Theta}$. In Section 4.5 we determined the apparent velocities for components B and B2, $\beta_{\rm app}$(B) = 3.74c ± 0.35c, $\beta_{\rm app}$(B2) = 1.43c ± 0.33c, and so we can combine $\beta\cos\Theta$ and $\beta_{\rm app}$ to place a constraint on the kinematics and orientation of the outer jet. The constraints to the jet velocity and source orientation are shown in Fig. 8. The results imply that the 3C 48 jet moves at $v > 0.85c$ along a viewing angle less than 35°.

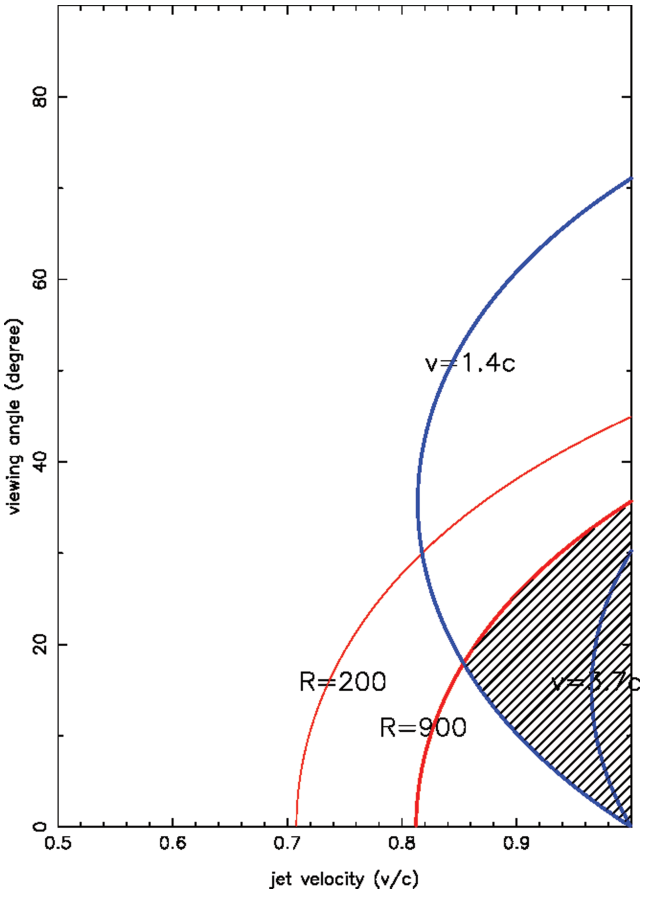

Figure 8. Constraints on source orientation and jet velocity from the VLBI observations. The shaded region indicates the parameter space constrained by the proper motion measurements and the jet-to-counterjet intensity ratios.

5.2 Helical radio jet structure

As discussed in Section 3.2, the bright jet knots define a sinusoidal ridge line. This is the expected appearance of a helically twisted jet projected on to the plane of the sky. Helical radio jets, or jet structure with multiple bends, can be triggered by periodic variations in the direction of ejection (e.g. precession of the jet nozzle) and/or random perturbations at the start of the jet (e.g. jet–cloud collisions). For example, the wiggles in the ballistic jets in SS 433 are interpreted in terms of periodic variation in the direction of ejection (Hjellming & Johnston 1981). Alternatively, small perturbations at the start of a coherent, smooth jet stream might be amplified by the Kelvin–Helmholtz (K-H) instability and grow downstream in the jet. In this case, the triggering of the helical mode and its actual evolution in the jet are dependent on the fluctuation properties of the initial perturbations, the dynamics of the jet flow and the physical properties of the surrounding ISM (Hardee 1987; Hardee 2003). In the following subsections, we consider these two models in more detail.

5.2.1 Model 1 – precessing jet

We use a simple precession model (Hjellming & Johnston 1981), taking into account only kinematics, to model the apparently oscillatory structure of the 3C 48 radio jet. Fig. 9 shows a sketch map of a 3D jet projected on the plane of the sky. The *x*- and *y*-axes are defined so that they point to the right ascension and declination directions, respectively. In the right-handed coordinate system, the *z*-axis is perpendicular to the XOY plane and the minus-*z* direction points to the observer. The jet axis is tilting towards the observer by an inclination angle of $(90 - \theta)$. The observed jet axis lies at a position angle α. In the jet rest frame, the kinematic equation of a precessing jet can be parametrized by jet velocity (V_j), half-opening angle of the helix cone (φ) and angular velocity (or, equivalently, precession period P).

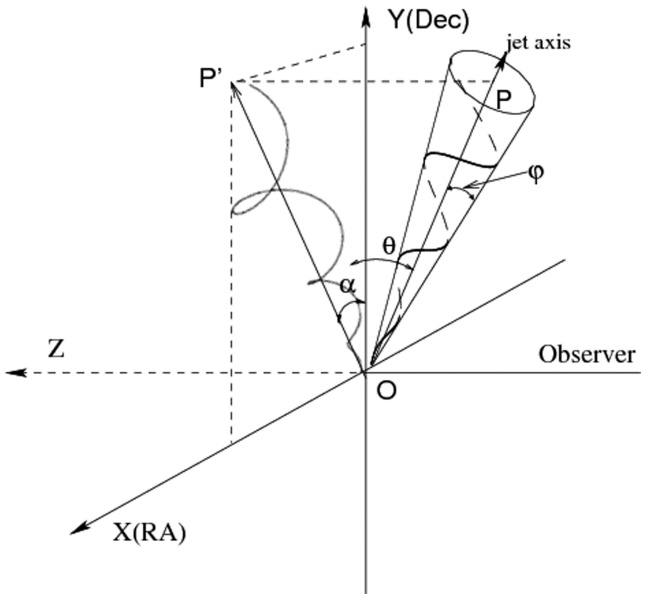

Figure 9. Sketch plot of the helical jet in 3C 48. The jet knots move on the surface of a helical cone. The XOY plane in the plot represents the projected sky plane, and the *x*-axis points to the right ascension direction and the *y*-axis to the declination direction. The *z*-axis is perpendicular to the plane of the sky and points away from the observer. The half of the opening angle of the helix is φ. The jet axis 'OP' is inclining by an angle of $(90 - \theta)$ with respect to the line of sight. The angle α between the OP' and *y*-axis is defined as the position angle in the 2D CLEAN image.

To simplify the calculations, we assume a constant jet flow velocity V_j, a constant opening angle φ of the helix and a constant angular velocity. We ignore the width of the jet itself, so we are actually fitting to the ridge line of the jet. The jet thickness does not significantly affect the fitting unless it is far wider than the opening angle of the helix cone. (We note that, although we have measured lower proper motion velocities in B and B2 than the velocity in the inner jet A2, this does not necessarily imply deceleration in the outer jet flow, since the brightening at B, and to some extent at B2, may arise mostly from stationary shocks; the proper motions of B and B2 thus represent a lower limit on the actual bulk motions of the jet.) We further assume that the origin of the precession arises from the central black hole and accretion disc system, so that (x_0, y_0, z_0) can be taken as zero. In the observer's frame, the jet trajectory shown in the CLEAN image can be acquired by projecting the 3D jet on the plane of the sky and then performing a rotation by an angle α in the plane of the sky so that the *y*-axis aligns to the north (declination) and the *x*-axis points to the east (right ascension). In addition to the above parameters, we need to define a rotation sign parameter $s_{\rm rot}$ ($s_{\rm rot} = +1$ means counterclockwise rotation) and jet side parameter ($s_{\rm jet} = +1$ means the jet moves towards the observer). Since we are dealing with the advancing jet, the jet side parameter is set to 1. Based on our calculations, we found that a clockwise rotation pattern ($s_{\rm rot} = -1$) fits the 3C 48 jet.

To estimate the kinematical properties of the precessing jet flow, we use the proper motion measurements of component A2 as an estimate of the jet velocity and orientation (Fig. 8). We have chosen a set of parameters consistent with the curve for $V_{\rm app,j} = 3.7c$ and a viewing angle of 17°. Other combinations of angles to the line of sight and velocities give qualitatively similar curves. For example, if we use a lower flow speed instead, a similar model structure can be produced by adjusting other parameters accordingly, e.g. by increasing the precessing period by the same factor. The high-resolution VLBI images (Fig. 3) show that the innermost jet aligns to the north. So an initial position angle $\alpha = 0$ should be a reasonable estimate. The VLBI images (Fig. 2) suggest that the position angle of the jet ridge line shows an increasing trend starting from the hot spot B. Moreover, we found that a model with a constant position angle does not fit simultaneously to both the inner and outer jets. To simplify the calculation, we introduced a parameter $\frac{{\rm d}\alpha}{{\rm d}r}$ to account for the increasing position angle in the outer jet.

The fitted jet ridge line is shown (thick green line) in the upper panel of Fig. 10 overlaid on the total intensity image. The assumed and fitted parameters are listed in Table 5. The modelled helix fits the general wiggling jet structure with at least two complete periods of oscillation. The fitted opening angle of 2.°0 suggests that the line of sight falls outside the helix cone. The initial phase angle ϕ_0 is loosely constrained; it is related to the reference time of the ejection of the jet knot, $\phi_0 = 2\pi t_{\rm ref}/P$. The fits suggest that the reference time is $t_{\rm ref} = -480$ yr. In the presence of the gradual tilting of the jet axis as well as the helical coiling around the jet axis, the fits most likely represent a superposition of the precession of the jet knots and the nutation of the jet axis, analogous to SS 433 (e.g. Katz et al. 1982; Begelman, King & Pringle 2006). The fitted period of 3500 yr is then a nutation period, about 0.4 times the dynamical time-scale of the jet, assuming a flow speed of $0.965c$, while the precession period is much longer. From the rate of the jet axis tilting, we estimate a precession period of $\sim 2 \times 10^5$ yr. The ratio of the estimated precession period to the nutation period is 57:1, 2.2 times the ratio in SS 433 (which has a 162 d periodic

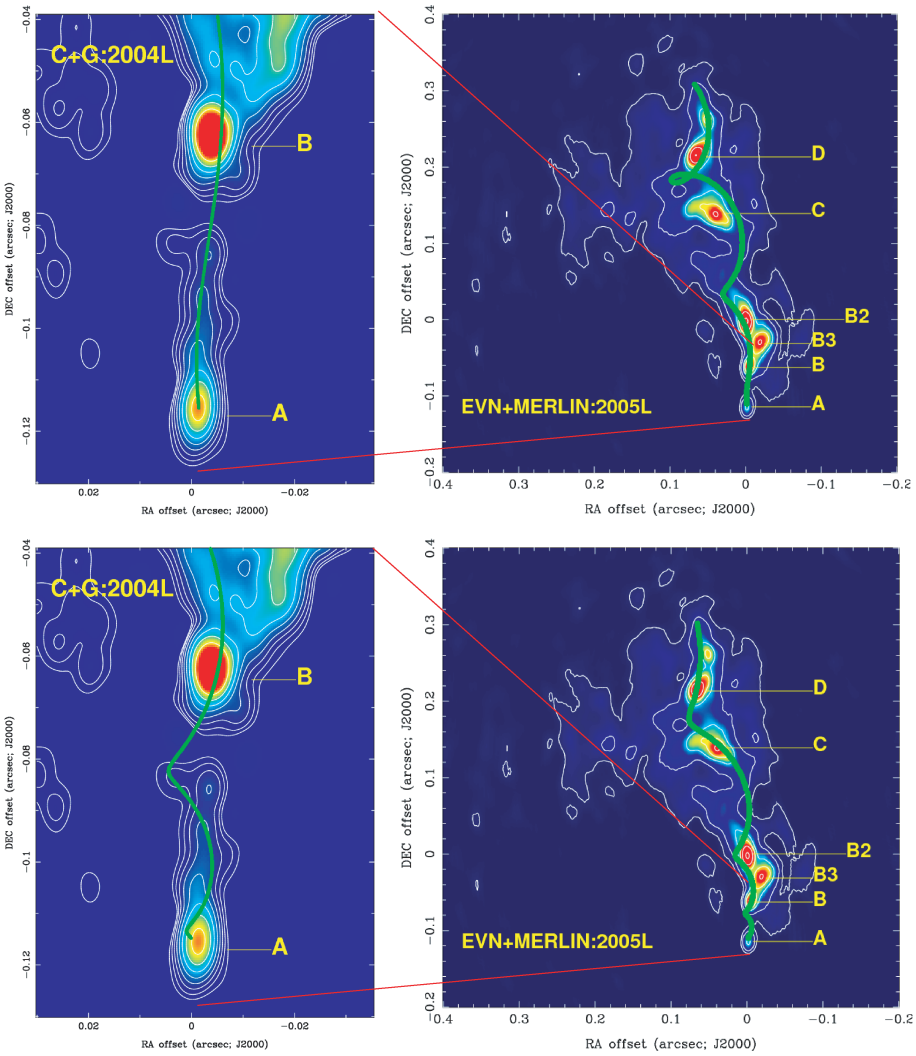

Figure 10. Helical-model fits overlaid on the total intensity images. Upper panel: the ridge line of the fitted precessing jet (thick green lines) overlaid on the 1.5-GHz VLBA (left) and 1.65-GHz EVN+MERLIN images. The CLEAN image parameters are referred to Table 2. Lower panel: the fitted jet trajectory (thick green line) from the K-H instability model.

precession and 6.3 d nodding motion; see Begelman et al. 2006 and references therein). The precessing jet model predicts a smooth structure on small scales, and a constant evolution of the wavelength so long as the jet kinetic energy is conserved and the helix cone is not disrupted (the opening angle of the helix cone is constant). However, the real 3C 48 jet probably does not conserve kinetic energy, as it is characterized by a disrupted jet and violent jet–ISM interactions. In particular, the inner-kpc jet is seen to be physically interacting with a massive gas system, and the observed blueshifted NIR clouds could be driven by the radio jet to move at velocities up to 1000 km s^{-1} (Chatzichristou et al. 1999; Gupta et al. 2005; Stockton et al. 2007). The 3C 48 radio jet thus might lose a fraction of its kinetic energy, resulting in a slowing down of the jet flow and the shrinking of the wavelength in the outer jet, assuming that the precessing periodicity is not destroyed.

5.2.2 *Model 2 – Kelvin–Helmholtz instabilities*

We next investigate the interpretation of a hydrodynamic or magnetized jet instability for a helical structure (Camenzind 1986; Hardee 1987). We used the simple analytic model described in Steffen et al. (1995) to fit to the helical jet trajectory in 3C 48. The kinematic equations of this toy model are solved on the basis of the conservation of kinetic energy $E_{\rm kin}$ and the specific momentum in the jet motion direction (case 2; Steffen et al. 1995). It is in fact identical to the isothermal hydrodynamic model (Hardee 1987) under the condition of a small helix opening angle. Model fitting with an adiabatically expanding jet can basically obtain a similar helical twisting jet as well, but the initial amplitude growth is much faster (Hardee 1987) than that of the isothermal jet. In this analysis, we confine our discussion to the isothermal case.

To make the calculations simple but not to lose generality, we used similar assumptions to those of model 1 on the jet kinematics and geometry. (We should note that although we used an apparent velocity $V_{\rm app,j}$ with same value in model 1, the jet speed $V_{\rm j}$ in the K-H model is the pattern speed, and therefore the real flow speed and the viewing angle in the K-H model are more uncertain than for the ballistic case.) In addition, we assume that the initial perturbations originate from a region very close to the central engine. The calculations thus start from an initial distance of zero along the jet axis and a small displacement r_0 in the rotation plane away from the jet axis. Moreover, we assumed an initial position angle $\alpha_0 = 0^\circ$

Table 5. Parameters of helical jet models.

	Assumed parameters			Fitted parameters				
	V_j (mas yr^{-1})	$90-\theta$ (°)	α_0 (°)	$d\alpha/dt$ (°/10^3 yr)	φ (°)	ψ_0 (°)	P (10^3 yr)	r_0 (mas)
Model 1[a]	0.164	17	0.0	1.8	2.0	50.0	3.5	–
Model 2[b]	0.164	17	0.0	1.6	1.5	50.0	0.366	1.8

Note. V_j: in the precessing model, V_j represents the flow speed in the observer's frame, taking into account relativistic aberration effects; in the K-H model, V_j denotes the pattern velocity. The velocity is expressed in terms of proper motion in order to agree with the coordinates used in CLEAN images.
θ: the angle between the jet axis and the sky plane.
α_0: the initial position angle of the jet axis, measured from north to east.
$d\alpha/dt$: the rate of change of position angle with time. In the precessing model, it gives an estimate of the angular velocity of the precession.
φ: half of the opening angle of the helix cone.
ψ_0: initial phase angle of the helical jet flow.
P: in 'model 1', the fitted *P* is actually the nutation period (see discussion in Section 5.2.1); in the K-H model, *P* represents an initial period for the triggered perturbations.
r_0: the initial radius where the K-H instability starts to grow.
[a]A precessing jet model.
[b]A helical-mode K-H instability model.

and again introduced a rate $d\alpha/dt$ to explain the eastward tilting of the jet axis. The half opening angle, which is a parameter to be fitted, is assumed constant. This assumption is plausible since the jet width seems not to change much within 0.5 arcsec, indicating that the trajectory of the jet is not disrupted even given the occurrence of a number of jet–ISM interactions. In addition to the above morphological assumptions, the model also assumes the conservation of specific momentum and kinetic energy E_{kin} along the jet axis. The conservation of specific momentum is equivalent to a constant velocity along the jet axis if mass loss or entrainment is negligible. The combination of the conservation of specific momentum and kinetic energy along the jet axis results in a constant pitch angle along the helical jet. Furthermore, the constant jet opening angle and pitch angle lead to a helical geometry in which the oscillatory wavelength linearly increases with time. The parameter r_0 controls how fast the wavelength varies (equation 12 in Steffen et al. 1995). The model describes a self-similar helical trajectory with a number of revolutions as long as the helical amplitude is not dampened too rapidly.

The modelled curve is exhibited in the lower panel of Fig. 10. The assumed and fitted parameters are listed in Table 5. As mentioned above, this K-H instability model predicts that, when the helical amplitude is not dampened and the opening angle φ is small ($\varphi \ll \arctan\frac{r_0}{\lambda_0}$), the oscillating wavelength (or period) along the jet axis increases linearly with time. The fits give an initial wavelength of 60 mas and an initial period of 370 yr. The period increases to 1.3×10^4 yr at the end of the plot window of 9000 yr. The fitted curve displays more oscillations in the inner part of the jet and smoother structure in the outer part, due to the decreasing angular velocity downstream. The initial transverse distance r_0 represents the location where the K-H instability starts to grow in the surface of the jet. It is associated with the varying rate of the wavelength. A value of $r_0 = 1.8$ mas corresponds to a projected linear distance of 9.2 pc off the jet axis. As discussed above, the major discrepancy between the helical model and the real 3C 48 jet could be the assumption of the conservation of kinetic energy E_{kin}. We have tried to fit the helical model without the conservation of kinetic energy but with conserved angular momentum, which is in principle similar to case 4 in Steffen et al. (1995). However, in this case, the modelled helix rapidly evolves into a straight line, and thus fails to reproduce the observed 3C 48 jet on kpc scales.

5.2.3 *Comparison of the two models*

Both two models give fits to the overall jet structure of 3C 48 within 0.45 arcsec with two to three complete revolutions, but they have some differences in detail. The helical shape of the precessing jet is a superposition of ballistic jet knots modulated by a nodding motion (nutation). In this case, the whole jet envelope wiggles out and shows a restricted periodicity. The observed jet structure displays a smooth shape on rather smaller scales. If, alternatively, the coherent, smooth jet stream is initially disturbed at the jet base, and is amplified by the K–H instability downstream in the jet, the jet stream itself is bent. The resulting helical jet flow rotates faster at the start and gradually slows down as it moves further away. If the twisted inner jet morphology detected at 1.5 and 4.8 GHz (Fig. 3) is real, this would support the K-H instability model. Further high-dynamic-range VLBI maps of the inner jet region could test this scenario.

In addition to the morphological discrepancy, the two models require different physical origins. In the precessing-jet model, ballistic knots are ejected in different directions which are associated with an ordered rotation in the jet flow direction in the vicinity of the central engine. If the precession results from a rotating injector at the jet base (see discussion in Worrall et al. 2007), the precession period of 0.2 million years requires a radius of $17 \times (\frac{M_\bullet}{10^9\,M_\odot})^{1/3}$ pc, assuming that the injector is in a Keplerian motion around the black hole. This size scale is much larger than the accretion disc, and so we may simply rule out the possibility of an injection from the rotating accretion disc. Instead, the long-term precession can plausibly take place in a binary supermassive black hole (SMBH) system or a tilting accretion disc (e.g. Begelman, Blandford & Rees 1980; Lu & Zhou 2005). For example, the precessing period caused by a tilting disc is $\sim 2 \times 10^5$ yr, assuming a 3×10^9 $M_\odot$ SMBH for 3C 48, a dimensionless viscosity parameter $\alpha = 0.1$ and the dimensionless specific angular momentum of the black hole $a = 0.5$ (Lu & Zhou 2005). In this scenario, the short-term nodding motion can then be triggered by the tidally induced torque on the outer brim of the

wobbling accretion disc, analogous to SS 433 (Katz et al. 1982; Bate et al. 2000).

On the other hand, the helical K-H instability modes can be triggered by ordered or random perturbations to the jet flow. The fits with model 2 give an initial perturbation period ∼370 yr, which leads to a radius of $\sim 0.25 \times (\frac{M_\bullet}{10^9\,\mathrm{M}_\odot})^{1/3}$ pc where perturbations take place. This radius is still larger than the size of the accretion disc, but at this size scale it is still plausible for the perturbations to be due to interactions between the jet flow and the broad-line-region clouds (e.g. 3C120; Gómez et al. 2000). However, the high Faraday depth and/or the possible internal depolarization structure in the radio core A makes it difficult to investigate this scenario through VLBI polarimetric measurements. In addition, K-H instabilities would not only produce simple helical modes, but also many other instability modes mixed together; the K-H interpretation of the oscillatory 3C 48 jet on both pc and kpc scales requires a selection of modes or a simple mix of low-order modes. However, it is difficult to see how these required modes are excited while others with higher growth rates are suppressed (see the discussion of the wiggling filament in NGC 315 by Worrall et al. 2007). Moreover, the K-H model does not have a ready explanation for the observed large-scale gradual bend of the jet axis. Simple kinematical models, such as a reflection by an oblique shock or a pressure gradient in the NLR ISM, may not be adequate to explain the bends of the robust ($\gtrsim 0.9c$) jet flow.

6 SUMMARY

We have observed 3C 48 at multiple frequencies with the VLBA, EVN and MERLIN with spatial resolutions between tens and hundreds of parsec. Our principal results may be summarized as follows.

(1) The total-intensity MERLIN image of 3C 48 is characterized by two components with comparable integrated flux density. A compact component aligns with the VLBI jet, while an extended envelope surrounds it. The extended emission structure becomes diffuse and extends towards the north-east at ∼0.25 arcsec from the nucleus. The extended component shows a steeper spectrum than the compact jet.

(2) In the VLBA and EVN images, the compact jet seen in the MERLIN image is resolved into a series of bright knots. Knot A is further resolved into two smaller features A1 and A2 in 4.8- and 8.3-GHz VLBA images. A1 shows a flat spectrum with spectral index $\alpha_{8.3}^{4.8} = -0.34 \pm 0.04$. A2 shows a steep spectrum with $\alpha_{8.3}^{4.8} = -1.29 \pm 0.16$, and may be identified with the inner jet. The brightness temperature of A1 is $>10^9$ K and much higher than the T_b of A2. The flux densities of A1 and A2 in epoch 2004 show a 100 and 60 per cent decrease compared with those in 1996. The high brightness temperature, flat spectrum and variability imply that A1 is the synchrotron self-absorbed core found close to the active nucleus.

(3) Comparison of the present VLBA data with those of 1996 January 20 strongly suggests that A2 is moving, with an apparent velocity of $3.7c \pm 0.4c$ to the north. Combining the apparent superluminal motion and the jet-to-counterjet intensity ratio yields a constraint on the jet kinematics and geometry: the jet is relativistic ($>0.85c$) and closely aligned to the line of sight ($<35^\circ$).

(4) We present for the first time VLBI polarization images of 3C 48, which reveal polarized structures with multiple subcomponents in component C. The fractional polarization peaks at the interface between the compact jet and the surrounding medium, perhaps consistent with a local jet-induced shock. The systematic gradient of the EVPAs across the jet width at C can be attributed to the combination of a gradient in the emission-weighted intrinsic polarization angle across the jet and possibly a systematic gradient in the RM. Changing magnetic-field directions are a possible interpretation of the RM gradient, but other alternatives cannot be ruled out. The fractional polarization of the hot spot B increases towards higher frequencies, from ∼1 per cent (1.6 GHz), ∼2.0 per cent (4.8 GHz) to 12 per cent (8.3 GHz). The relatively low degree of polarization at lower frequencies probably results from a unresolved Faraday screen associated with the NLR clouds and/or the internal depolarization in the jet itself. Hot spot B has a higher RM than C, which can perhaps be attributed to a stationary shock in the vicinity of B. The core A at all frequencies is unpolarized, which may be the result of a tangled magnetic field in the inner part of the jet.

(5) The combined EVN+MERLIN 1.65-GHz image and 1.5-GHz VLBA images show that the bright knots trace out a wave-like shape within the jet. We fitted the jet structure with a simple precession model and a K-H instability model. Both models in general reproduce the observed oscillatory jet trajectory, but neither of them is able to explain all the observations. More observations are required to investigate the physical origin of the helical pattern. Further monitoring of the proper motion of the inner jet A2 should be able to constrain the ballistic motion in the framework of the precessing jet. High-resolution VLBI images of the inner jet region will be required to check whether or not the jet flow is oscillating on scales of tens of mas, which might give a morphological means of discriminating between the two models. Sophisticated simulations of the jet would be needed to take into account the deceleration of the jet flow due to kinetic energy loss via jet–cloud interaction and radiation loss, but these are beyond the scope of this paper.

ACKNOWLEDGMENTS

TA and XYH are grateful for partial support for this work from the National Natural Science Foundation of PR China (NSFC 10503008, 10473018) and Shanghai Natural Science Foundation (09ZR1437400). MJH thanks the Royal Society (UK) for support. We thank Mark Birkinshaw for helpful discussions on the jet kinematics. The VLBA is an instrument of the National Radio Astronomy Observatory, a facility of the US National Science Foundation operated under cooperative agreement by Associated Universities, Inc. The EVN is a joint facility of European, Chinese, South African and other radio astronomy institutes funded by their national research councils. MERLIN is a National Facility operated by the University of Manchester at Jodrell Bank Observatory on behalf of the UK Science and Technology Facilities Council (STFC).

REFERENCES

Akujor C. E., Spencer R. E., Zhang F. J., Davis R. J., Browne I. W. A., Fanti C., 1991, MNRAS, 250, 215
An T., Hong X. Y., Wang W. H., 2004, Chinese J. Astron. Astrophys., 4, 28
Bate M. R., Bonnell I. A., Clarke C. J., Lubow S. H., Ogilvie G. I., Pringle J. E., Tout C. A., 2000, MNRAS, 317, 773
Begelman M. C., Blandford R. D., Rees M. J., 1980, Nat, 287, 307
Begelman M. C., King A. R., Pringle J. E., 2006, MNRAS, 370, 399
Briggs D. S., 1995, PhD thesis, New Mexico Institute of Mines and Technology
Canalizo G., Stockton A., 2000, ApJ, 528, 201
Camenzind M., 1986, A&A, 156, 137
Chatzichristou E. T., Vanderriest C., Jaffe W., 1999, A&A, 343, 407
Condon J. J., Cotton W. D., Greisen E. W., Yin Q. F., Perley R. A., Taylor G. B., Broderick J. J., 1998, AJ, 115, 1693
Cotton W. D., Fanti C., Fanti R., Dallacasa D., Foley A. R., Schilizzi R. T., Spencer R. E., 1997a, A&A, 325, 479

Cotton W. D., Dallacasa D., Fanti C., Fanti R., Foley A. R., Schilizzi R. T., Spencer R. E., 1997b, A&A, 325, 493
Cotton W. D., Dallacasa D., Fanti C., Fanti R., Foley A. R., Schilizzi R. T., Spencer R. E., 2003, A&A, 406, 43
Fanti C., 2009, Astron. Nachr., 330, 120
Fanti C., Fanti R., Parma P., Schilizzi R. T., van Breugel W. J. M., 1985, A&A, 143, 292
Fanti R., Fanti C., Schilizzi R. T., Spencer R. E., Nan R. D., Parma P., van Breugel W. J. M., Venturi T., 1990, A&A, 231, 333
Fanti C., Fanti R., Dallacasa D., Schilizzi R. T., Spencer R. E., Stanghellini C., 1995, A&A, 302, 317
Feng W. X., An T., Hong X. Y., Zhao J.-H., Venturi T., Shen Z.-Q., Wang W. H., 2005, A&A, 434, 101
Gómez J.-L., Marscher A. P., Alberdi A., Jorstad S. G., García-Miró C., 2000, Sci, 289, 2317
Gómez J.-L., Marscher A. P., Jorstad S. G., Agudo I., Roca-Sogorb M., 2008, ApJ, 681, L69
Greenstein J. L., 1963, Nat, 197, 1041
Gupta N., Srianand R., Saikia D. J., 2005, MNRAS, 361, 451
Hardee P. E., 1987, ApJ, 318, 78
Hardee P. E., 2003, ApJ, 597, 798
Hjellming R. M., Johnston K. J., 1981, ApJ, 246, L141
Katz J. I., Anderson S. F., Grandi S. A., Margon B., 1982, ApJ, 260, 780
Kellermann K. I., Pauliny-Toth I. I. K., 1969, ApJ, 155, L71
Krips M., Eckart A., Neri R., Zuther J., Downes D., Scharwachter J., 2005, A&A, 439, 75
Lu J.-F., Zhou B.-Y., 2005, ApJ, 635, L17
Mantovani F., Mack K.-H., Montenegro-Montes F. M., Rossetti A., Kraus A., 2009, A&A, 502, 61
Matthews T. A., Bolton J. G., Greenstein J. L., Munch G., Sandage A. R., 1961, Sky Telescope, 21, 148
Murgia M., Fanti C., Fanti R., Gregorini L., Klein U., Mack K.-H., Vigotti M., 1999, A&A, 345, 769
Nan R. D., Schilizzi R. T., Fanti C., Fanti R., 1991, A&A, 252, 513
Nan R. D., Cai Z. D., Inoue M., Kameno S., Schilizzi R. T., Fanti C., Fanti R., 1992, PASJ, 44, 273
O'Dea C. P., 1998, PASP, 110, 493
O'Dea C. P. et al., 2002, ApJ, 123, 2333
Owsianik I., Conway J. E., Polatidis A. G., 1998, A&A, 336, L370 [Correction added after online publication 17 December 2009: added reference]
Peacock J. A., Wall J. V., 1982, MNRAS, 198, 843
Readhead A. C. S., Taylor G. B., Xu W., Pearson T. J., Wilkinson P. N., Polatidis A. G., 1996, ApJ, 460, 612 [Correction added after online publication 17 December 2009: added reference]
Shen Z.-Q., Jiang D. R., Kameno S., Chen Y. J., 2001, A&A, 370, 65
Simard-Normandin M., Kronberg P. P., Button S., 1981, ApJS, 45, 97
Simon R. S., Readhead A. C. S., Moffet A. T., Wilkinson P. N., Booth R., Allen B., Burke B. F., 1990, ApJ, 354, 140
Spencer R. E. et al., 1991, MNRAS, 250, 225
Stanghellini C., O'Dea C. P., Dallacasa D., Baum S. A., Fanti R., Fanti C., 1998, A&AS, 131, 303
Steffen W., Zensus J. A., Krichbaum T. P., Witzel A., Qian S. J., 1995, A&A, 302, 335
Stockton A., Ridgway S. E., 1991, AJ, 102, 488
Stockton A., Canalizo G., Fu H., Keel W., 2007, ApJ, 659, 195
Taylor G. B., Myers S. T., 2000, VLBA Scientific Memo 26. National Radio Astronomy Observatory, Socorro, NM
van Breugel W., Miley G., Heckman T., 1984, AJ, 89, 5
Wilkinson P. N., Spencer R. E., Readhead A. C. S., Pearson T. J., Simon R. S., 1984, in Fanti R., Kellermann K. I., Setti G., eds, Proc. IAU Symp. 110, VLBI and Compact Radio Sources. Kluwer, Dordrecht, p. 25
Wilkinson P. N., Tzioumis A. K., Akujor C. E., Benson J. M., Walker R. C., Simon R. S., 1990, in Zensus J. A., Pearson T. J., eds, Parsec-Scale Radio Jets. Cambridge Univ. Press, Cambridge, p. 152
Wilkinson P. N., Tzioumis A. K., Benson J. M., Walker R. C., Simon R. S., Kahn F. D., 1991, Nat, 352, 313
Worrall D. M., Hardcastle M. J., Pearson T. J., Readhead A. C. S., 2004, MNRAS, 347, 632
Worrall D. M., Birkinshaw M., Laing R. A., Cotton W. D., Bridle A. H., 2007, MNRAS, 380, 2
Xiang L., Reynolds C., Strom R. G., Dallacasa D., 2006, A&A, 454, 729
Zuther J., Eckart A., Scharwachter J., Krips M., Straubmeier C., 2004, A&A, 414, 919

This paper has been typeset from a TEX/LATEX file prepared by the author.